Effects of super–shear rupture speed

on the high frequency content of S–waves

investigated using spontaneous dynamic rupture models

and isochrone theory

A. Bizzarri[1], P. Spudich[2]

[1] Istituto Nazionale di Geofisica e Vulcanologia,

Sezione di Bologna, Bologna, Italy

[2] U. S. Geological Survey,

Menlo Park, CA, USA

Abstract

This paper achieves three goals: 1) It demonstrates that crack tips governed by friction laws including slip–weakening, rate– and state–dependent laws, and thermal pressurization of pore fluids, propagating at super–shear speed have slip velocity functions with reduced high frequency content compared to crack tips traveling at sub–shear speeds. This is demonstrated using a fully dynamic, spontaneous, 3–D earthquake model, in which we calculate fault slip velocity at nine points (locations) distributed along a quarter–circle on the fault where the rupture is traveling at super–shear speed in the in–plane direction and sub–shear speed in the anti–plane direction. This holds for a fault governed by the linear slip–weakening constitutive equation, by slip–weakening with thermal pressurization of pore fluid and by rate– and state–dependent laws with thermal pressurization. The same is also true even assuming a highly heterogeneous initial shear stress field on the fault. 2) Using isochrone theory we derive a general expressions for the spectral characteristics and geometric spreading of two pulses arising from super–shear rupture, the well–known Mach wave, and a second lesser known pulse caused by rupture acceleration. 3) The paper demonstrates that the Mach cone amplification of high frequencies overwhelms the deamplification of high frequency content in the slip velocity functions in super–shear ruptures. Consequently, when earthquake ruptures travel at super–shear speed, a net enhancement of high frequency radiation is expected, and the alleged "low" peak accelerations observed for the 2002 Denali and other large earthquakes are probably not caused by diminished high frequency content in the slip velocity function, as has been speculated.

theory, numerical simulations.

1. Introduction

The problem of the rupture propagation at speeds greater that shear wave velocity has received the increasing interest of theoretical and numerical studies, laboratory experiments and observations of real–world events. Using analytical models of non–spontaneous, purely in–plane (mode II) crack Burridge (1973), Freund (1979), Broberg (1994, 1995) and Samudrala et al. (2002) demonstrated that rupture can stably propagate at super–shear rupture velocity. At the same time numerical simulations showed that spontaneous ruptures governed by a linear slip–weakening friction law (Andrews, 1976a; Das and Aki, 1977a; Das, 1981; Bizzarri et al., 2001 in the 2–D, purely in–plane case and Day, 1982; Madariaga and Olsen, 2000; Bizzarri and Cocco, 2005 (BC05 in the following); Day et al., 2005 in the 3–D one) as well as spontaneous ruptures obeying to rate– and state–governing laws (Okubo, 1989 in the 2–D case and BC05 in the 3–D one) exhibit, for carefully chosen values of governing parameters, a jump from sub– to super–shear rupture velocities.

On the other hand, pioneering laboratory experiments made by Wu et al. (1972) and by Johnson et al. (1973) showed that super–shear stick–slip motion occurred after a stable sliding. More recently it has been found (Rosakis et al., 1999; Xia et al., 2004) that shear cracks from either projectile impact loading or shear loading with exploding–wire–nucleation can propagate at intersonic speed in homalite.

In spite of this profusion of analytical, numerical and laboratory evidence it is well known that observations of crustal earthquakes have revealed that most ruptures tend to propagate

with an average velocity that is about 80% of the shear wave velocity (e. g. Heaton, 1990). However, there are a few earthquake ruptures which appear to have propagated with a velocity greater that the shear wave velocity: the M6.5 1979 Imperial Valley, California, EQ (Olson and Apsel, 1982; Archuleta, 1984; Spudich and Cranswick, 1984), the M7.4 1999 Kocaeli (Izmit), Turkey, EQ (Bouchon et al., 2000, 2001), the M7.2 1999 Ducze, Turkey, EQ (Bouchon et al., 2001), the M8.1 2001 Kokoxili (Kunlun), Tibet, EQ (Bouchon and Vallee, 2003; Bhat et al., 2007); the M7.9 2002 Denali, Alaska, EQ (Ellsworth et al., 2004; Dunham and Archuleta, 2004; Aagaard and Heaton, 2004; Dunham and Archuleta, 2005); the M6.0 2004 Parkfield, California, EQ (Liu et al., 2006), and the 1906 San Francisco, California, earthquake (Song et al., 2007). However, there is some debate regarding the robustness of the conclusions made in above–mentioned papers (see for instance Archuleta, 1984; Bouin and Bernard, 1994; Delouis et al., 2002). Much uncertainty about the observation of super–shear rupture is mainly due to the lack of sufficient strong motion records (Bhat et al., 2007).

The above list suggests that large (M > 7.1) strike–slip earthquakes have an increased tendency to rupture at super–shear speed, and more importantly, M ~ 8 strike–slip earthquake might preferentially rupture at super–shear speed. Because these earthquakes are potentially the most damaging, it is important to determine whether super–shear rupture speed might have some systematic effect on ground motions. Three competing effects have been identified. Both Spudich and Frazer (1984; henceforth SF84) and Bernard and Baumont (2005; henceforth BB05) have noted that super–shear ruptures emit a Mach cone having enhanced high frequencies. BB05 further noted that sustained super–shear propagation can radiate a locally planar or conical wave front having less geometric spreading than that radiated from sub–shear rupture. Spudich and Oppenheimer (1986, their Figure 8) found that in ruptures with highly

variable rupture velocity, most of the high frequency radiation comes from numerous very compact loci of super–shear rupture. On the other hand, Ellsworth et al. (2004) and BB05 have noted that in classical fracture mechanical models, crack tip singularities emit diminished high frequency motion when traveling at super–shear speeds, which might nullify the Mach cone enhancement of high frequencies. Ellsworth et al. (2004) specifically proposed this to explain the reduction of high frequency motion at Pump Station 10 during the Denali earthquake, compared to the predictions of ground motion prediction relations. More generally, newly developed ground motion prediction relations based on data from the recent large earthquakes listed above (e.g. Abrahamson and Silva, 2008; Boore and Atkinson, 2008; Campell and Bozorgnia, 2008; Chiou and Youngs, 2008) show that peak acceleration reaches a limit at high magnitudes, which may be related in part to the super–shear rupture velocity in these earthquakes, although the 1999 Chi–Chi, Taiwan, earthquake, which was sub–shear, also shows this limited ground motion.

There is theoretical evidence suggesting that super–shear ruptures emit diminished high frequency motion. From the analytical solutions found by Burridge (1973) of a non–spontaneous (i.e., with prior imposed constant rupture velocity), purely in–plane, self–similar problem, Andrews (1976b), using a simple Coulomb fracture criterion (i.e., without governing law), predicts that the slip velocity pulse v is of the form

$$v(t) \propto \left(t - t_a\right)^{-a^{(A)}} H\left(t - t_a\right) \tag{1}$$

where $H(.)$ is the Heaviside function and t_a is the arrival time of the crack at the chosen distance from the initiation where v is calculated. In equation (1) the exponent $a^{(A)}$ is equal to

1/2 in the sub–shear regime (formally when the rupture velocity v_r is lower than or equal to the Rayleigh velocity v_R); in the super–shear one (i.e., if $v_S \leq v_r \leq v_P$) $a^{(A)}$ increases from 0 at $v_r = v_S$ up to 1/2 for v_r equal to the Eshelby speed ($v_E \underset{df}{=} \sqrt{2} v_S$; Eshelby, 1949) and then decreases down to 0 when $v_r = v_P$. This implies that slip velocity pulse will have less high frequency when the crack is traveling with super–shear rupture speed and more high frequency when it is sub–shear[1]. This simply because $(t - t_a)^{-0} H(t - t_a)$ has less high frequency (Fourier amplitude spectrum $\propto \omega^{-1}$) than $(t - t_a)^{-1/2} H(t - t_a)$ (Fourier amplitude spectrum $\propto \omega^{-1/2}$). Andrews (1976b) also showed that slip velocity pulses in smoothed fracture models might also show the same modification of their high–frequency components, although he did not specify a constitutive laws.

One of the goals of the present paper is to see if the above conclusion about the Fourier spectrum of slip velocity is valid also in the case of a fully spontaneous, *truly* 3–D rupture developing on a planar fault governed by different constitutive equations. It is well known (see for instance Madariaga and Olsen, 2000; BC05) that in the 3–D rupture problem v_r increases continuously up to the P–wave speed without having any forbidden range (from v_R to v_S), typical of the purely in–plane rupture problems. In the light of this fact, the result of Andrews tells us nothing about the exponent $a^{(A)}$ — and therefore about the high frequency content of the slip velocity pulse — for $v_R \leq v_r \leq v_S$. In addition to this limitation, Andrews' conclusion is related to a problem in which, by definition, there is no coupling between the two components of fault slip, fault slip velocity and traction, as on the contrary our model considers (see BC05 for more details). A second goal is to use kinematic isochrone theory (Bernard and Madariaga,

1984; SF84) to investigate the effects of super–shear rupture speed on the Fourier spectrum of far–field pulses generated by the spontaneous rupture calculation. We break our study into dynamic and kinematic parts for several reasons. First, the use of isochrone theory enables us to derive some mathematical insight into the nature and types of radiated pulses, insights that would not emerge from a completely numerical calculation. Second, it is computationally infeasible to perform a completely numerical finite difference calculation in our broad frequency band at far–field receivers. Third, we are attempting to separate a complicated phenomenon into individual component parts that are more easily understood. We are not proposing that such a mixed dynamic/kinematic approach is suitable for modelling ground motions in the far–field from arbitrary heterogeneous rupture models.

In summary, this paper achieves two main goals: 1) it demonstrates that crack tips governed by friction laws including slip–weakening, rate– and state–dependent laws, and thermal pressurization of pore fluids, propagating at super–shear speed have slip velocity functions (SVFs) with reduced high frequency content, and 2) it demonstrates that the Mach cone amplification of high frequencies overwhelms the diminution of high frequency content in the SVFs in such rupture models. Consequently, when earthquake ruptures travel at super–shear speed, a net enhancement of high frequency radiation is expected, and the alleged "low" peak accelerations observed for the 2002 Denali and other large earthquakes are probably not caused by diminished high frequency content in the SVF, contrary to the speculations of Ellsworth et al. (2004) and BB05.

We achieve goal 1 in two ways. First, we compare the spectra of SVFs at fault points in the anti–plane (sub–shear) and in–plane (super–shear) directions at equal radii from the hypocenter of a rupturing fault with spatially uniform properties. We have done this, rather

than comparing in–plane points in two separate rupture models, one everywhere sub–shear and one somewhere super–shear, because creation of the two rupture models for the latter test requires variation of so many parameters between the two rupture models (i.e., stress drops, slip–weakening distances, etc.) that the comparison is difficult to interpret. Second, we compare the spectra of SVFs at super–shear and sub–shear points in a highly heterogeneous rupture model.

We achieve goal 2 by deriving the spectral amplification of S–waves expected during super–shear rupture compared to sub–shear, and then applying that amplification to the slip velocity spectra observed at fault points having super–shear rupture speed. By the term "spectral amplification" we mean the modification of some spectrum, such as a slip velocity spectrum or a ground displacement spectrum, by a multiplicative function of frequency, typically ω^{γ}, where γ can be positive or negative. The spectral amplification might result from Mach cone effects or diminution of the crack tip singularity, for example.

2. Isochrone theory and super–shear rupture speed

2.1. Theoretical development

In this section we show that super–shear rupture speed boosts the Fourier amplitude spectrum (FAS) of the far–field ground motion radiated from a kinematic slip model (a prescribed slip function having realistic wavenumber spectrum) by a factor of frequency between $\omega^{1/2}$ and ω^{1} in the frequency band governing peak acceleration, approximately 10–50 Hz, compared to sub–shear rupture of the same slip distribution. Of course, BB05 and Dunham and Archuleta (2005) have already shown (in the far– and near–field, respectively)

that super–shear rupture speed in models having spatially smooth slip causes the radiated pulse to be temporally differentiated compared to the sub–shear case. However, since isochrone theory as implemented by Bernard and Madariaga (1984) and SF84 is a high frequency far–field approximation, it is worthwhile to verify that the approximation is valid in the 10–50 Hz range rather than only above 1000 Hz. Note that isochrone theory can be extended to give the exact broad–band response including near–field terms in a whole space (Joyner and Spudich, 1994).

SF84 noted that enhanced high frequencies can be radiated from places on a fault where there are stationary points (extrema and saddle points) of the arrival time function, i.e. points where isochrone velocity is singular. Sustained super–shear propagation causes a local minimum of arrival time, the situation investigated by BB05. However, acceleration of rupture speed to super–shear causes a saddle point of the arrival time function, also yielding a high frequency pulse which is less well known. Since no such stationary points exist for sub–shear rupture velocity, there are no sub–shear equivalents to these pulses.

The characteristics of these two pulses can be derived theoretically. Rewriting equation (8) of SF84 with a slight change of notation, the *i*–component of far–field S–wave displacement is:

$$u_i(t) = \dot{f}_r(t) * \iint_A F_i(x, y) \delta(t - T(x, y)) \, \mathrm{d}x \, \mathrm{d}y \tag{2}$$

where A is the fault area, (x,y) is a position on A, $\dot{f}_r(t)$ is the slip velocity time function, T is the S–wave arrival time function (sum of rupture time and S–wave arrival time), and $F_i = \mathbf{s_r} \cdot \mathbf{G_i^S}$ is the product of the slip vector and the Green's function amplitude vector (see SF84 for exact definitions of these terms). (2) can be rewritten as

$$u(t) = f_r(t) * \iint\limits_A F(x,y)\delta'(t - T(x,y))\,\mathrm{d}x\,\mathrm{d}y = f_r(t) * I(t) \tag{3}$$

where $I(t)$ is the integral over the fault and where we have dropped the i subscript. Note that $I(t)$ contains all the effects of wave propagation and the kinematic rupture model, except for the SVF. Denoting temporal Fourier transforms by overbars, (3) may be written as $\bar{u} = \bar{f}_r \bar{I}$ or $\bar{u} = \bar{\dot{f}}_r \bar{I}$. $I(t)$ is the ground velocity pulse if $\dot{f}_r(t) = \delta(t)$. Burridge (1963) investigated the behavior of $I(t)$ at relative minima, maxima, and saddle points of T. Let $T_{,xy} = \left.\dfrac{\partial}{\partial x}\dfrac{\partial}{\partial y}T\right|_{x_O,y_O}$, let (x_O,y_O) be the coordinate of the stationary point of T, and let $T_O \equiv T(x_O,y_O)$. For a minimum at (x_O,y_O) (the case of $T_{,xx} > 0$, $T_{,yy} > 0$, $T_{,xy} = 0$), Burridge expanded T in a Taylor series around (x_O,y_O), and retaining only the leading term he found:

$$I(t) \cong 2\pi F(x_O,y_O)\left|T_{,xx}T_{,yy}\right|^{-1/2}\delta(t - T_O). \tag{4}$$

Therefore,

$$u(t) \cong 2\pi F(x_O,y_O)\left|T_{,xx}T_{,yy}\right|^{-1/2}f_r(t - T_O) \tag{5}$$

This corroborates BB05's result that the far field displacement pulse from sustained super–shear rupture propagation has the same time function as the fault slip at high frequency. However, the term $\left|T_{,xx}T_{,yy}\right|^{-1/2}$ contains the combined directivity and geometric spreading of the pulse, and will vary depending on the receiver location. Equation (5) generalizes BB05's result to arbitrary super–shear rupture time distributions. BB05's equation (A5), showing that

the pulse from a linear super–shear rupture front does not decay with distance, and their equation (A7), showing cylindrical spreading of a pulse from a circularly expanding super–shear rupture front, are easily derived from (5).

When rupture accelerates gradually from sub– to super–shear speed, arrival time T can have a saddle point at (x_O, y_O), and in this case Burridge found

$$I(t) \cong -\frac{1}{\pi} F(x_O, y_O) 2\pi \left| T_{,xx} T_{,yy} \right|^{-1/2} (t - T_O)^{-1} \tag{6}$$

Therefore,

$$u(t) \cong -2\pi F(x_O, y_O) \left| T_{,xx} T_{,yy} \right|^{-1/2} \left[\frac{1}{\pi} \int \frac{f_r(t' - T_O)}{t - t'} \, dt' \right] \tag{7}$$

The term inside brackets is the definition of the Hilbert transform $\mathcal{H}[.]$ of $f_r(t - T_O)$, so the displacement pulse from a saddle point is the Hilbert transform of the slip function at (x_O, y_O):

$$u(t) \cong -2\pi F(x_O, y_O) \left| T_{,xx} T_{,yy} \right|^{-1/2} \mathcal{H}\left[f_r(t - T_O) \right] \tag{8}$$

Because the FAS of the Hilbert transform is the same as the FAS of its argument, the saddle point pulse (from rupture acceleration to super–shear) has exactly the same spectral enrichment as the pulse from an arrival time minimum (sustained super–shear pulse). Note also that the expression for directivity and geometric spreading of the pulse from an accelerating rupture front has the same form in (8) as the constant speed pulse in (5).

2.2. A computed example

In this section we wish to demonstrate the amount of spectral enrichment expected from super–shear rupture propagation in a simple kinematic model with realistic slip heterogeneity. To verify that the spectral predictions of the above section persist in a more realistic kinematic rupture model, we created a slip distribution with a k^{-2} spectral fall–off at high radial wavenumber (yielding an ω^{-2} displacement spectrum) and a correlation distance of 6 km, following equation (A11) of Mai and Beroza (2002) derived from slip distributions of real earthquakes. BB05 (their Figure 6) have done a similar calculation, but we show our result in the spectral rather than the time domain. Our slip distribution was biased positive so that it had no negative slip and was tapered linearly to zero at its edges over distances of 2–5 km (Figure 1). The SVF was chosen to be $\dot{f}_r(t) = \delta(t)$. The rupture front was a straight line parallel to the y axis moving in the $+x$ direction at either constant sub– or super–shear speed (Figures 1a and b) or accelerating to super–shear speed (Figure 1c). We used isochrone theory to calculate ground displacement pulses (specifically $I(t)$, because $\dot{f}_r(t) = \delta(t)$) from this slip model for three rupture velocity cases, constant sub–shear velocity, constant super–shear velocity, and acceleration to super–shear speed. Time windows for Fourier analysis were chosen to exclude artificial pulses generated by isochrones either crossing corners of the fault or being tangent to the fault edges. The calculated pulses correspond well to the theoretical expectations. In the super–shear case (second row of Figure 1) the arrival time function has a relative minimum at $T_O = 13.4$ s, and the ground velocity is dominated by a delta function at 13.4 s although much smaller radiation from the fault continues to arrive until 19.0 s, corroborating the expectation from (5) that the ground velocity is dominated by the super–shear critical point, and that

ground velocity should look like the slip velocity. The third row shows the case of accelerating rupture leading to a saddle point at $T_O = 17.1$ s, which causes a $(t - T_O)^{-1}$ singularity, as expected from $(8)^{(2)}$. The top row shows the case of sub–shear rupture speed, in which the arrival time function has no stationary point. Radiated ground motions are much smaller in this case, and the spectral fall–off of the velocity pulse (Figure 2) is proportional to ω^{-1}, as expected, compared to the flat spectra from the two super–shear cases (dashed and thin lines in Figure 2). (For our choice of $\dot{f}_r(t)$, a slip heterogeneity spectrum proportional to $k^{-\alpha}$ causes a velocity spectrum proportional to $\omega^{-\alpha+1}$ for sub–shear rupture. The ground velocity spectrum of the super–shear pulses is dominated by the singularity and is largely unaffected by the slip heterogeneity spectrum. For the case of $\alpha = 1.5$, which is the smallest permissible value of the wavenumber exponent (Andrews, 1980), the sub–shear S–wave spectrum would be proportional to $\omega^{-1/2}$, while the super–shear spectrum would still be flat.)

In summary, the spectrum of the super–shear S–wave pulse (more specifically, the spectrum of $I(t)$) is enriched by a factor of at least $\omega^{1/2}$ compared to the sub–shear spectrum, and is enriched by a factor of ω when the slip heterogeneity spectrum is proportional to k^{-2} at high wavenumber. This spectral amplification will persist for any other choice of $\dot{f}_r(t)$, as long as the spectrum of $\dot{f}_r(t)$ varies sufficiently slowly on the fault to allow this term to be taken outside the integral in (2). We will comment on the validity of this approximation later. Like BB05, we note that the physical causes of high frequency ground motion differ between the sub–shear and super–shear cases, and that isochrone theory is applicable in both cases in the far field. In the sub–shear case, spatial variations of slip and rupture velocity on the fault cause

high frequency motions that radiate to the far field (see for example (16) of SF84), and the spectrum of these motions is controlled by the heterogeneity spectrum on the fault. In the super–shear case, the high frequency ground motion spectrum is only slightly affected by the slip heterogeneity spectrum, and is primarily controlled by the spectrum of the SVF. Of course, our rupture front in these models is quite simple, and more complicated rupture propagation, possibly having several regions of super–shear speed, would be expected in a heterogeneous slip model such as this. In such a more realistic model, we expect that each region of super–shear speed would radiate pulses like those of Figure 1b and 1c.

3. The fault model

3.1. The numerical scheme

In this paper we solve the fundamental elasto–dynamic equation, free from body forces, using the *truly* 3–D (i.e., not simply mixed–mode; both components of fault slip are found from one vectorial constitutive relation, so that rake rotation can be calculated realistically), second–order in space and in time, finite difference, conventional–grid based code presented in BC05. The problem is fully dynamic, in the sense that we consider inertia in the whole time window of numerical computations and we do not use the Radiation Damping Approximation (Rice, 1993). We recall here the basics of the model and mainly the differences with respect to BC05; the reader can refer to that paper for all the details and for the analysis of convergence and stability.

Referring to Figure 3, in the Cartesian coordinate system $Ox_1x_2x_3$ the spatial computational domain $\Omega^{(FD)}$ is discretized using parallelepipeds having edges parallel to coordinate axes. In

$\Omega^{(FD)}$ the vertical plane $\mathcal{S} = \{\mathbf{x} \mid \mathbf{x} = (x_1, x_2^f, x_3)\}$ contain the fault Σ (now is $\Sigma \subseteq \mathcal{S}$ and not $\Sigma = \mathcal{S}$ as in BC05), having normal unit vector $\hat{\mathbf{n}} \mathbin{/\mkern-5mu/} \hat{\mathbf{x}}_2 \equiv (0,1,0)$.

For sake of simplicity we restrict numerical experiments presented and discussed in the remainder of this paper to the special case of a linearly elastic rheology: a Regular–Node is therefore governed by the Hooke's law. On the contrary, on the fault surface Σ we may prescribe different constitutive relations, as described in the following. The implementation of the fault boundary condition (FBC) is done using the traction–at–split–node (TSN) technique, and the introduction of the fault governing law is discussed in detail in BC05. The plane $x_3 = 0$ is the free surface and the other five planes are absorbing and not cyclic or fixed as in B05. In that way, as we reduce (but do not completely eliminate) the pollution of radiation reflected by or interacting with domain boundaries, we can study wide temporal windows and relatively large fault planes with a very fine spatial discretization in a computationally feasible domain, since we can reduce the extension of $\Omega^{(FD)}$ in the direction normal to the fault. All numerical details about absorbing boundary conditions (ABCs) are given in Appendix A. In principle, this will obviously limit the recording of particle motions only in a narrow region surrounding the fault, but this is not a problem, as in the following of the paper we are interested in the on–fault time series. Because of the narrowness of our computational domain in the direction normal to the fault, the influence of the boundary conditions affects our on–fault time series in three (models A to C) of the four models presented here. However, the influence of the boundary does not affect our inferences of the relative spectral levels of sub–shear and super–shear slip velocities, and we present a model (model D in Section 7) unaffected by boundary conditions that supports this belief.

3.2. The fault governing law

We can regard a constitutive equation as an analytical relation describing the dependence of the fault friction τ on various physical observables (see equation (3.2) in BC05). The shear traction $\mathbf{T}^{(\hat{\mathbf{n}})}$ acting on Σ ($\left\|\mathbf{T}^{(\hat{\mathbf{n}})}\right\| = \sqrt{\sigma_{21}^2 + \sigma_{23}^2}$,$\{\sigma_{2j}\}_{j\,=\,1,\,3}$ being the components of the stress tensor) is subjected to the boundary condition $\mathbf{T}^{(\hat{\mathbf{n}})} = \tau$.

In tribology there is no general consensus about the law that best describes an earthquake rupture (see Ohnaka, 2003 and Bizzarri and Cocco, 2006c for a review); in the literature two main classes of friction laws have been introduced: slip–dependent laws and rate– and state–dependent laws. In this paper we will adopt the linear slip–weakening (SW in the following) law (Ida, 1972; Andrews, 1976a, 1976b):

$$\tau = \begin{cases} \tau_u - (\tau_u - \tau_f)\dfrac{u}{d_0} & ,u < d_0 \\ \tau_f & ,u \ge d_0 \end{cases} \qquad (9)$$

where $\tau_u = \mu_u \sigma_n^{eff}$ and $\tau_f = \mu_f \sigma_n^{eff}$ are the maximum, yield (or also static) stress and the kinetic, residual (or also dynamic) level, respectively and u is the fault slip (no opening or material interpenetration is allowed in the numerical experiments presented and discussed in this paper, as in BC05). The time required for the traction to drop from τ_u down to τ_f defines the breakdown zone time (see also Figure 1a in Cocco and Bizzarri, 2002). σ_n^{eff} is the effective normal stress, i.e., the modulus of the normal traction $\mathbf{\Sigma}^{(\hat{\mathbf{n}})} = -\sigma_n^{eff}\hat{\mathbf{n}} = -(\sigma_n - p_{fluid})\hat{\mathbf{n}}$ (being σ_n the normal stress (namely $-\sigma_{22}$) and p_{fluid} the pore fluid pressure; stresses are assumed to be negative for compression), while d_0 is the scale length that controls the decrease of frictional

resistance with increasing cumulative fault slip, a behavior commonly observed in laboratory experiments in a variety of specimens, including intact, saw–cut, and jointed rocks, as well as overconsolidated clay samples. The weakening behavior is also described (Okubo, 1989; Cocco and Bizzarri, 2002; Bizzarri and Cocco, 2003) within the framework of the more elaborate rate– and state–dependent friction laws (Ruina, 1983; Roy and Marone, 1996, among many others).

4. Results for a dry fault

4.1. The model configuration

In this section we will discuss results obtained assuming that fault friction obeys equation (9) in the case of constant effective normal stress; in the following we will refer to this configuration as model A. The computational domain $\Omega^{(FD)}$ is discretized by adopting a homogeneous mesh of cubes and the medium is Poissonian and elastic everywhere except on the fault surface (i.e., in the split–node area) Σ (see Table 1 for details), where the initial traction $\mathbf{T_0} = \tau_0 \left(\cos(\varphi(x_1, x_3, 0)), 0, \sin(\varphi(x_1, x_3, 0)) \right)$ acts at $t = 0$, φ being the azimuth (i.e., the rake angle), which is assumed to be initially 0°.

Nucleation is obtained following the procedure introduced for the 2–D problems by Bizzarri et al. (2001). In a circular region centered on the hypocenter H and having radius r_{nucl}, the fault strength τ^{fault} is the minimum of the value arising from equation (9) and that obtained from a time–weakening function

$$\tau^{(\text{TW})} = \begin{cases} \left[\mu_u - (\mu_u - \mu_f) \dfrac{(t - t_{force})}{t_0} \right] \sigma_n^{\ eff} & , t - t_{force} < t_0 \\[4mm] \mu_f \sigma_n^{\ eff} & , t - t_{force} \geq t_0 \end{cases} \tag{10}$$

where $t_{force} = t_{force}(x_1, x_3)$ is the onset time in a generic fault point (x_1, x_3) of a non–spontaneous

rupture propagating at the forcing velocity v_{force} ($t_{force}(x_1, x_3) \equiv \dfrac{\sqrt{\left(x_1 - x_1^{\ H}\right)^2 + \left(x_3 - x_3^{\ H}\right)^2}}{v_{force}}$)

and t_0 is a characteristic time. We chose the values of $v_{force} = 0.87 \, v_R = 2400$ m/s and $t_0 = 0.1$ s.

In order to ensure a spontaneous rupture propagation outside the initialization patch, the

nucleation radius r_{nucl} has to be greater than the critical value (G is the rigidity of the medium)

$$r_c = \frac{7\pi}{24} G \frac{\tau_u - \tau_f}{\left(\tau_0 - \tau_f\right)^2} d_0 \tag{11}$$

(Day, 1982)[3].

4.2. Transition from sub– to super–shear rupture velocities

In Figure 4 we plot the rupture speed v_r on the fault plane; due to the homogeneity of the

model the rupture propagates symmetrically with respect to H and therefore only a portion of Σ

is displayed. For clarity of presentation in Figure 4 we plot v_r only up to time $t = 1.29$ s, in

order to better emphasize region where rupture front accelerates to super–shear rupture

velocities. At a generic point of the fault (x_1, x_3) the failure time $t_r(x_1, x_3)$ is defined as the instant

of time at which it has a slip velocity greater than a threshold (or limiting) value v_l, assumed to

be equal to 0.01 m/s. This value is two orders of magnitude smaller than the typical peak slip velocity which is attained in the numerical experiments presented in this paper. Our value of v_l is compatible with that (1 mm/s) used by Day et al. (2005) to capture what happens in most of the breakdown zone in numerical experiments on homogeneous faults where the rupture always accelerates to a seismic regime. From the rupture time array it is trivial to calculate the rupture speed v_r, which is simply the inverse of the slowness[4]:

$$v_r(x_1, x_3) = \frac{1}{\left\| \nabla_{(x_1,x_3)} t_r(x_1,x_3) \right\|} \tag{12}$$

We choose the value if 0.01 m/s for v_l because the high frequency radiation from the fault is generated by the rapid increase of the fault slip velocity at the crack tip and by the peak in slip velocity. This is in agreement with Madariaga (1983), who observed that in crack models the high–frequency energy is radiated from the crack tip of a propagating rupture. Therefore we need a critical value that tends to precede the rapid increase in fault slip velocity by a constant time interval. The value ($v_l = 0.1$ m/s) adopted in previous papers (Belardinelli et al., 2003; Antonioli et al., 2006; Bizzarri and Belardinelli, 2007) to discriminate between aseismic and seismic regimes of a fault subjected to an external stress perturbation is too high for use in the present work and, moreover, some slipping fault points will never reach this value if the stress drop is low.

From Figure 4 we can see that rupture accelerates to super–shear velocities, as expected (see for instance Andrews, 1976b and Dunham, 2007) for a low value of strength parameter ($S \underset{\mathrm{df}}{=} \dfrac{\tau_u - \tau_0}{\tau_0 - \tau_f}$; Das and Aki, 1977a, 1977b; $S = 0.8$ in model A). In the direction of the

pre–stress $\mathbf{T_0}$ (namely in the in–plane direction) the rupture accelerates up to super–shear velocity, reaching a value (4209 m/s) which is very close the Eshelby speed ($v_E = 4243$ m/s for our parameters); on the contrary, in the anti–plane direction v_r always remains sub–shear, as already numerically demonstrated by BC05. Moreover, it is evident from Figure 4 and from Table 2 that there are intermediate regions where v_r increases from sub– to super–shear rupture velocity, passing through the rupture velocity interval forbidden in 2–D (e.g. Andrews, 1976b). BC05 showed that in a *truly* 3–D fault model, such as that considered here, there is a complex coupling of the purely in–plane and the purely anti–plane modes of propagation, accompanied by a rake variation during rupture propagation, especially in the breakdown zone, and this is different from the behavior that occurs in self–similar elliptical crack enlargement, where the slip is everywhere parallel to the pre–stress direction (Burridge and Willis, 1969).

4.3. Spectra of the fault slip velocity

In Figure 5 we plot the magnitude of the Fourier amplitude spectra (FAS) of the fault slip velocity time series at nine locations considered (black triangles in Figure 4). All locations in this numerical experiment are at a distance of 3000 m from H (this guaranties that results are not affected by the imposed nucleation procedure) and at different azimuths with respect to H (see Table 2). As a consequence of the linear SW governing law with constant effective normal stress, all the locations experience the same stress drops (both static, $\Delta\tau_s \underset{\mathrm{df}}{=} \tau_0 - \tau_f$, and breakdown, $\Delta\tau_b \underset{\mathrm{df}}{=} \tau_u - \tau_f$), but different rupture velocities. SVFs for locations 1, 5, and 9 are shown in Figure 6, left column. In this and all other models, the FAS is the spectrum of the magnitude of the fault slip velocity time series. The same basic procedure **was** used to calculate

the FAS for all models, although some parameters differed. All locations' slip acceleration time series were terminated by a cosine–taper of duration t_{dur} starting at a delay t_{start} after the first non–zero value (i.e., the onset time). The termination of the acceleration time series was chosen to exclude the back–propagating healing phases from unslipped parts of the models, external to the TSN area Σ. The tails of the tapered accelerations were padded with zeros and integrated to velocity, shown by the black lines in Figure 6. The tails of these velocities were gradually cosine tapered to zero (not shown in Figure 6), and the tapered slip velocities were normalized to have one meter of total cumulative slip (not shown), a value that may be associated with a M ~ 7 event. In the case of model A we used t_{start} = 0.5 s and t_{dur} = 0.1 s for the acceleration taper and t_{start} = 0.3 s and t_{dur} = 0.7 s for the velocity taper (left column in Figure 6).

The results seen in Figure 5 for model A are generally duplicated for the other models. Spectra (solid lines) agree at low frequency but diverge above 10 Hz. In all models' calculations a numerical oscillation occurs at some frequency, that frequency always being the lowest for anti–plane locations (see the arrow at 80 Hz for locations 7, 8, and 9 in Figure 5) and highest for in–plane locations (about 180 Hz for location 1, not visible in Figure 5). These oscillations are visible in Figure 6, left column. Because of the numerical oscillation, the in–plane and anti–plane locations' spectra cannot be compared in the band marked "not valid" on the figure, although the in–plane spectra are usually valid well into that band[5].

The general result in Figure 5, as will be seen in the other models, is that in the band where the FAS diverge (10–40 Hz in this case), the FAS of the pure in–plane location (1) is in the middle of the group, the location closest to the super– to sub–shear transition (3 in this case) has the lowest FAS, and the FAS of the sub–shear locations (4 to 9) exceed those of the

super–shear. This verifies the predictions of Burridge (1973) and Andrews (1976b) that super–shear crack tips should have less abrupt slip velocity onsets than sub–shear tips. As in the models presented below (Sections 5 and 6), the location with the lowest FAS experiences the largest rake rotation within the breakdown zone.

The *relative* quantitative effect of super–shear enhancement of high frequency radiation can be shown compactly on Figure 5. Because $\bar{\bar{u}} = \bar{\dot{f}}_r \bar{I}$, multiplication of each of the spectra (solid lines) by the spectrum of $I(t)$ gives the spectrum of ground motion from the kinematic model corresponding to $I(t)$ with each SVF. Let $\bar{I}_>(\alpha)$ be the spectrum of $I(t)$ for a super–shear rupture velocity and slip distribution having wavenumber spectrum $k^{-\alpha}$, and let $\bar{I}_<(\alpha)$ be the same for sub–shear rupture velocity. From Figure 2 we know $\bar{I}_>(2)/\bar{I}_<(2) = \omega$, and from the discussion we know that $\bar{I}_>(1.5)/\bar{I}_<(1.5) = \omega^{1/2}$. In other words, for $\dot{f}_r(t) = \delta(t)$, super–shear rupture speed boosts the radiated spectrum of a sub–shear k^{-2} slip model by a factor of ω, and it boosts the spectrum of a $k^{-1.5}$ slip model by $\omega^{1/2}$. Consequently, to see the *relative* spectral levels of ground motions from sub– and super–shear rupture, we must boost the super–shear slip velocity spectra by a factor of ω or $\omega^{1/2}$, for k^{-2} or $k^{-1.5}$ slip models, respectively.

The dashed and dotted FAS in Figure 5 are the FAS of super–shear locations (solid lines for 1, 2, and 3) scaled by ω and $\omega^{1/2}$, respectively, to simulate the spectral enhancement of the radiated S–waves expected for super–shear rupture speed compared to sub–shear ruptures for slip heterogeneity spectra that follow k^{-2} and $k^{-1.5}$ at high wavenumber, respectively (Figure 2). They show that the spectral enhancement expected from super–shear propagation exceeds the diminution of spectral amplitude caused by super–shear reduction of the crack tip singularity.

Consequently, Figure 5 contradicts the speculation of Ellsworth et al. (2004) and BB05 that a super–shear induced reduction of the crack–tip singularity caused the Pump Station 10 accelerations to be "low".

In the preceding (and subsequent) discussion we make an implicit (and physically reasonable) assumption that allows us to use isochrone theory, which assumes spatially slowly varying slip SVFs, and numerical results from spatially uniform initial conditions, to infer the characteristics of radiation from heterogeneous ruptures. Real–world ruptures will have spatial variations of slip amplitude and rupture velocity. There will be some high–slip patches over which the rupture front travels at sub–shear speed and some other patches over which there is super–shear speed. Because the slip is not uniform in these patches, they will radiate high frequency motions to the far field, governed by isochrone theory. The assumption we have made is that the *differences* between the FAS of sub–shear and super–shear SVFs obtained from the solution of the spontaneous problem will approximate the *differences* between the FAS of the SVFs of the sub–shear and super–shear patches, respectively. In other words, if we observe that the FAS of our sub–shear locations has more high frequency content than the FAS of our super–shear locations, the same will be true of small slip patches in heterogeneous models that slip at sub–shear and super–shear speed. In Section 7 we present a heterogeneous spontaneous rupture model that supports this assumption.

5. FAS in case of temporally varying effective normal stress

The second configuration we consider (model B, Table 1) includes time–variable effective normal stress due to pore fluid pressure changes. The latter, in turn, are caused by the physical phenomenon of the thermal pressurization (frictional heat enhances the pore fluid migration)

for which the analytical solution is given by Bizzarri and Cocco (2006a, 2006b). More explicitly, we consider equation (9) of Bizzarri and Cocco (2006a), from which we can clearly see that, in each fault node and at every time level it is necessary to store in memory all the value of fault slip velocity and of fault traction in that fault point for all previous time levels. This cause a very massive computer memory request, much larger than in the case of model A (for which this time convolution is not necessary, p_{fluid} being constant through time); we have therefore considered a different spatio–temporal discretization in this case. However, we maintained the depth of the hypocenter H unchanged with respect to model A, and consequently all effects of the free surface are exactly the same in the two models. Thermal pressurization parameters are the same as those listed in Table 1 of Bizzarri and Cocco (2006a).

From the distribution of the rupture speed reported in Figure **7** (the calculation is plotted only up to time $t = 1.21$ s for clarity, as done in Figure 4) it is evident that also in this case the crack tip bifurcates and the rupture accelerates up to super–shear velocity. It is interesting to note that the initial value of the strength parameter S is 1.5 in this case and without the inclusion of thermal pressurization we would have only sub–shear velocity in the spatio–temporal domain considered. As already pointed out by Bizzarri and Cocco (2006a, 2006b), the variation of pore fluid pressure and consequently the progressive decrease of the effective normal stress will cause a temporally variable S which increases (with respect to the dry case) the dynamic load of the slipping points, causing in turn the rupture front bifurcation and the transition to super–shear velocities, and enhances the instability of the fault, increasing the peak fault slip velocity. Now the maximum v_r is well above v_E and the fault region where the crack tip is traveling with super–shear velocity is wider (compare Figures 4 and **7**, plotted

for clarity using the same color scale); now also locations located up to azimuth of − 45° (where the propagation modes II and III are identically operating) have $v_r > v_S$.

We plot in Figure 8 the FAS in the nine fault locations listed in Table 2 and marked in Figure 7; all the locations on are placed at the same distance from H considered in model A and the depths are (practically) the same. Owing to the greater numerical demands of this calculation, time series were much shorter, necessitating different taper parameters. Acceleration taper parameters were $t_{start} = t_{dur} = 0.11$ s, and velocity taper parameters were $t_{start} = 0.5$ s and $t_{dur} = 2.0$ s. Untapered and acceleration–tapered velocity time series (prior to the final velocity taper) are shown in Figure 6, middle column. In this case we can see the effects of numerical oscillation at frequencies ranging from about 80 Hz for in–plane locations down to 25 Hz for location 9 at − 90° azimuth (Figures 6 and 8). We can compare FAS only up to a frequency of 10 Hz, below which the time evolutions are unaffected by spurious oscillations[6]. Owing to the brevity of the acceleration–tapered time series and to the 10 Hz upper limit, for this model there is a very narrow frequency band in which the various locations' FAS can be compared, perhaps 3–10 Hz. Consequently, the results of this model must be regarded as tentative, although they are in general agreement with both other models.

As in the case of model A, we can see that the fault slip velocity FAS of sub–shear locations are higher than super–shear ones in the 3–10 Hz band: the sequence of the locations with increasing FAS is: 5, 4, 3, 2, 1, 6, 7, 8, 9 (underlined numbers are super–shear locations). As in the model A, the super–shear location closest to the super– to sub–shear transition, location 5 at − 45° azimuth, has the lowest FAS. As in Figure 5, the dashed and dotted FAS in Figure 8 are the FAS of super–shear locations (solid lines for 1 to 5) multiplied by ω and $\omega^{1/2}$

respectively, to simulate the spectral enhancement expected in the radiated S–waves for slip heterogeneity spectra that follow k^{-2} and $k^{-1.5}$ at high wavenumber, respectively. In the band below 10 Hz the FAS corrected for super–shear pulse enhancement (1 to 5, dotted and dashed lines) exceed the FAS of the sub–shear locations (6 to 9, solid lines).

6. FAS of rate and state model with thermal pressurization

All the results presented in previous sections refer to faults governed by linear SW law (equation (9)). We have also considered a case (model C; parameters are listed in Table 1) in which we adopt the Dieterich–Ruina law (Linker and Dieterich, 1992; Bizzarri and Cocco, 2006a, 2006b):

$$\tau = \left[\mu_* + a \ln\left(\frac{\upsilon}{\upsilon_*} \right) + b \ln\left(\frac{\Psi \upsilon_*}{L} \right) \right] \sigma_n^{eff}$$

$$\frac{\mathrm{d}}{\mathrm{d}t} \Psi = 1 - \frac{\Psi \upsilon}{L} - \left(\frac{\alpha_{LD} \Psi}{b \sigma_n^{eff}} \right) \frac{\mathrm{d}}{\mathrm{d}t} \sigma_n^{eff}$$

(13)

where the temporal variation of the effective normal stress, caused by thermal pressurization of pore fluid, are coupled with the state variable Ψ by way of the dimensionless constant α_{LD}. Nucleation is obtained through the spontaneous evolution of the state variable, as described by Bizzarri et al. (2001) and by BC05; the model parametrization, as well as the locations locations, are identical to model B. The resulting rupture velocity distribution on the fault plane (Figure 9) is very similar to that obtained in models A and B (see Figures 4 and 7), showing a concentration of fault points experiencing super–shear velocity in a cone having axis coincident with x_1 (see also Table 2).

Even in the case of constant governing parameters and pre–stress, the presence of thermal pressurization (model B) as well as the adoption of rate– and state–dependent friction (model C) cause the stress drop to be not uniform on the fault plane (see for instance Bizzarri and Cocco, 2006a, 2006b; Tinti et al., 2005, their Figure 2b), unlike model A.

The beginning of the slip velocity was deemed to start at 0.015 s before the time when v exceeded 0.1 m/s, in order to capture the slow initial acceleration of slip velocity. An acceleration taper of duration $t_{dur} = 0.1$ s was applied to the end of each slip acceleration trace, where the total duration of the acceleration trace was not allowed to exceed 0.6 s (Figure 6, right column). This procedure varied slightly from the tapering of models A and B, by using a different length acceleration–tapered time series for each fault location. We did this because the SVFs for model C were much lower frequency than the other models' SVFs, and prolonging the retained time series gave us a broader usable FAS bandwidth. FAS in Figure 10 confirm what we have previously observed in models A and B. In the frequency range 5–20 Hz sub–shear locations are richer in high frequency content than super–shear ones; the sequence of the locations having increasing value of FAS amplitude is: 3, 4, 2, 1, 5, 6, 7, 8, 9 (underlined numbers indicate again locations where rupture speed is super–shear). As in previous models, location 4 (the super–shear location closest to the sub–shear one) has the lowest FAS. On the contrary, the purely anti–plane location (9) exhibits the higher FAS, indicating that the increase in fault slip velocity is faster that in case of other locations. Finally, we would remark that the knee at 30 Hz in the FAS of location 9 is due to numerical oscillations and we can probably trust numerical results up to 20 Hz. As in models A and B, the FAS of super–shear locations (1 to 4) scaled by ω and $\omega^{1/2}$ (dashed and dotted lines, respectively) to simulate the spectral enhancement expected in the radiated S–waves for super–shear pulse enhancement exceed the

FAS of the sub–shear locations (5 to 9, solid lines).

7. Results for a highly heterogeneous initial shear stress model

We have calculated the spontaneous rupture of model D, having a highly heterogeneous stress field, that supports two assumptions made in this paper, namely 1) that the *differences* between the FAS of sub–shear and super–shear SVFs obtained from the solution of the spontaneous problem in homogeneous stress models (e.g. A, B and C) will approximate the *differences* between the FAS of the SVFs of the sub–shear and super–shear patches, respectively, in heterogeneous models, and 2) that the influence of boundary conditions is not biasing our observation that sub–shear FAS are richer in high frequencies than super–shear FAS. In model D the linear SW friction law with constant effective normal stress is assumed on the fault; as in all previous models, the initial shear stress field has only one non–null component (i.e., $\varphi = 0$), but now it follows a self–similar distribution (following equation (B12) in Frankel and Clayton, 1986), with a correlation distance (parameter a in equation (B3) of Frankel and Clayton, 1986) of 400 m. The obtained stress distribution is such that in some patches of the fault the maximum yield stress is exceeded and therefore rupture initiation occurs and then the rupture will spontaneously propagate.

Figure 11 shows the distribution on the fault plane of the initial stress (Figure 11a), rupture times (Figure 11b), and local rupture speeds (Figure 11c). Model D is not a realistic model of an earthquake because slip initiates at several locations simultaneously. However, this attribute ensures that almost all of the fault ruptures before the arrival time, 0.62 s, of the first P

reflected from the x_2 boundary 1.6 km from the fault surface. Hence, the SVFs of all points more than 1.6 km from any boundary are uncontaminated until 0.62 s.

Our goal was to calculate average sub– and super–shear FAS for locations that were not near a hypocenter and that were unaffected by reflections from any boundary. Model D has many points that ruptured at either sub– or super–shear speed (Figure 11c). We saved the SVFs of 99 locations on the whole fault surface. From these we excluded SVFs from locations that were less than 1.6 km from the free surface and from the edges of the slipped zones. We retained locations that ruptured in the time window that started mid–way into the rupture process (between 0.16 and 0.32 s), and for these locations we calculated FAS on the first 0.32 s of their SVFs, using the usual acceleration taper strategy with $t_{start} = 0.19$ s, $t_{dur} = 0.13$ s and a subsequent velocity taper with $t_{start} = 0.5$ and $t_{dur} = 2.0$ s. (The selected time window and duration admit a maximum of 0.02 s of tapered reflected P for some locations, but the "broad" time window was necessary to get enough sub–shear locations.) We retained the six sub–shear locations having rupture velocity v_r in the range 2.0 to 2.76 km/s, and we retained the seven super–shear locations having $v_r > 3.4$ km/s. The average FAS of each group is shown in Figure 11d. The SVFs usually have a numerical oscillation at about 70 Hz. Owing to the short duration (0.32 s) of the retained SVFs, we believe that the spectra are controlled by padding and tapering assumptions below about 6 Hz. Therefore, the valid bandwidth for comparing sub– and super–shear FAS is about 6–30 Hz.

From Figure 11d we can see that the average sub–shear (blue) FAS is about a factor of 1.5 or 2 above the super–shear FAS (red). This factor is slightly smaller than the very approximate factor of 3 found in models A, B, and C. However, model D spectra support both of our assumptions: 1) that sub–shear FAS have greater high frequency content than super–shear FAS

in heterogeneous models as well as in homogeneous models A, B, and C, and 2) that the relationship of the FAS is not affected by the boundary condition. Model D confirms our conclusion that when the super–shear FAS are multiplied by ω or by $\omega^{1/2}$, owing to the Mach cone effect, the Mach cone effect has a stronger amplification than the diminution caused by the reduction of the super–shear FAS crack tip "singularity".

8. Discussion and conclusions

In this paper we have used results from Burridge (1963) to derive a general expression for the geometric spreading of far–field super–shear S pulses. We have shown that the same spectral amplification is expected in a pulse radiated from sustained super–shear propagation (i.e., a pulse caused by a minimum of arrival time) and in a pulse radiated from an accelerating rupture (i.e., caused by a saddle point of arrival time), compared to a pulse from the same slip distribution and SVF rupturing at sub–shear speed. That spectral amplification should be proportional to ω or $\omega^{1/2}$, respectively, for slip heterogeneity spectra that follow k^{-2} and $k^{-1.5}$ at high wavenumber.

We have also shown that in a fully dynamic, spontaneous and *truly* 3–D earthquake model with uniform friction the slip velocity in fault points where rupture edge is traveling with super–shear speed has less high frequency content than that calculated in points where rupture velocity is sub–shear. This holds for a fault governed by the linear, or classical, slip–weakening constitutive equation (model A), by slip–weakening with temporally variable effective normal stress (caused by the thermal pressurization of pore fluid; model B) and by the fully non–linear rate– and state–dependent laws (model C). This also holds when a highly heterogeneous initial shear stress field is assumed on the fault (model D). These conclusions agree with previous

inferences based on a non–spontaneous (i.e., with prior imposed constant rupture velocity), purely in–plane, self–similar problem without constitutive law.

The application of the ω or $\omega^{1/2}$ amplification to our super–shear slip velocity FAS causes them to exceed the FAS of the sub–shear locations, suggesting that S pulses from super–shear rupture should be richer in high frequency than pulses from sub–shear rupture, despite the diminution of the crack–tip singularity caused by super–shear propagation. This implies that the "low" (compared to previous relations) peak accelerations predicted by newly developed ground motion prediction relations for large magnitude events (e.g. Abrahamson and Silva, 2008; Campell and Bozorgnia, 2008; Boore and Atkinson, 2008; Chiou and Youngs, 2008) are probably not caused by super–shear rupture.

Footnotes

[1] Here words "less" and "more" refer to the spectra of pulses that have been normalized in order to have the same value at low frequency.

[2] Note that for this case, the slip distribution is the same as for the other cases, but the portion between – 10 and 0 km has been removed to exclude a potentially interfering pulse from a local minimum of the arrival time function, located at about – 5 km along strike.

[3] For a Poissonian medium (as considered in this study) for the same constitutive parameters, the value arising from equation (11) is greater than the critical distance derived in purely in–plane case by Andrews (1976b), $L_c^{(II)} = \dfrac{2}{\pi} G \dfrac{\lambda + G}{\lambda + 2G} \dfrac{\tau_u - \tau_f}{(\tau_0 - \tau_f)^2} d_0$, where λ is the first Lamé constant. This type of nucleation, with a proper choice of v_{force} and t_0, guarantees a gradual transition between the non–spontaneous and the spontaneous regime.

[4] The quantity in equation (12) is what Day (1982) called local, or tangent, rupture speed, to distinguish it from the average, or secant, rupture speed, which in turn is expressed as

$v'_r (x_1, x_3) = \dfrac{\sqrt{(x_1 - x_1^H)^2 - (x_3 - x_3^H)^2}}{t_r(x_1, x_3)}$. In general v_r' is everywhere less than v_P — as a consequence of principle of causality — and it may be sub–shear even if v_r is super–shear.

[5] Our assumption is that a solution is unaffected by oscillations at frequencies somewhat lower than those at which the oscillations appear, as shown by the frequency bands marked "not valid" in Figures 5, 8, and 10. Even if the problem is non–linear, in our simulations the oscillations never become large enough to introduce fault slip velocity zeros (i.e., early arrest of sliding). Additionally, the (small) reflections originating from the borders of the TSN region

Σ (behaving like an impenetrable barrier and generating healing phases) were excluded by choosing a time window that did not include them.

[6] We determined the 10 Hz limit by inspecting the FAS of a signal we created that closely simulated the numerical oscillation time series, consisting of a sine wave with time–varying frequency and exponentially decaying envelope.

Appendix A. Domain boundary conditions

The plane $x_3 = 0$ is the free surface, that is the traction–free condition is imposed:

$\mathcal{T}_j^{(\hat{\mathbf{n}})} = n_i \sigma_{ij} = 0$. Taking into account that $\hat{n}$ // $\hat{\mathbf{x}}_3 \equiv (0,0,1)$ the previous requirement is simply:

$\sigma_{3j} = 0$.

The remaining five planes are absorbing (i.e., non reflecting) and not cyclic or fixed as in BC05. A node belonging to one of such an absorbing plane is a special node for which the Absorbing Boundary Condition (ABC) is applied. We impose the ABCs on each component $l = 1, 2, 3$ of the particle velocity $\dot{\mathbf{U}}$ accordingly to the formula (cfr. Peng and Toksöz, 1994, 1995; Moczo, 1998):

$$
\begin{aligned}
\dot{U}_{1jk_l}^m = \quad & A_{01}\dot{U}_{2jk_l}^m & + \quad & A_{02}\dot{U}_{3jk_l}^m \\
+ \quad A_{10}\dot{U}_{1jk_l}^{m-1} + \quad & A_{11}\dot{U}_{2jk_l}^{m-1} & + \quad & A_{12}\dot{U}_{3jk_l}^{m-1} \\
+ \quad A_{20}\dot{U}_{1jk_l}^{m-2} + \quad & A_{21}\dot{U}_{2jk_l}^{m-2} & + \quad & A_{22}\dot{U}_{3jk_l}^{m-2}
\end{aligned}
\tag{A.1}
$$

where superscript m denotes the actual time level and subscripts j and k indicate the position of the node along x_1 and x_3, respectively. Equation (A.1) is valid for the left boundary $x_1 = 0$ (i.e., $i = 1$), while for the right boundary $x_1 = x_{1_{end}}$ (i.e., $i = i_{end}$) the condition (A.1) becomes:

$$
\begin{aligned}
\dot{U}_{i_{end}jk_l}^m = \quad & A_{01}\dot{U}_{i_{end}-1\,jk_l}^m & + \quad & A_{02}\dot{U}_{i_{end}-2\,jk_l}^m \\
+ \quad A_{10}\dot{U}_{i_{end}jk_l}^{m-1} + \quad & A_{11}\dot{U}_{i_{end}-1\,jk_l}^{m-1} & + \quad & A_{12}\dot{U}_{i_{end}-2\,jk_l}^{m-1} \\
+ \quad A_{20}\dot{U}_{i_{end}jk_l}^{m-2} + \quad & A_{21}\dot{U}_{i_{end}-1\,jk_l}^{m-2} & + \quad & A_{22}\dot{U}_{i_{end}-2\,jk_l}^{m-2}
\end{aligned}
\tag{A.2}
$$

In equations (A.1) and (A.2), that are analogously writable for boundaries $x_2 = 0$, $x_2 = x_{2_{end}}$ and $x_3 = x_{3_{end}}$, coefficients $\{A_{pq}\}_{p,q\ =\ 1,2,3}$ depend on the choice of ABC scheme (e. g. Clayton and Engquist, 1977; Reynolds, 1978; Emerman and Stephen, 1983; Higdon, 1991; Peng and Toksöz, 1994, 1995; Liu and Archuleta, 2000, personal communication). The best absorption is obtained in our cases adopting the following coefficient matrix A_{pq}

$$\begin{pmatrix} 0 & -Q_X - R_X & -Q_X R_X \\ -Q_T + R_X & Q_X R_X - Q_T R_X - Q_{XT} - 1 & Q_X - R_X Q_{XT} \\ Q_T R_X & Q_T + R_X Q_{XT} & Q_{XT} \end{pmatrix} \tag{A.3}$$

where:

$$Q_X = \frac{W_b\left(1 + N_I\right) - N_I}{\left(1 + N_I\right)\left(1 - W_b\right)}$$

$$R_X = (1 - w_{CFL})/(1 + w_{CFL})$$

$$Q_T = \frac{W_b\left(1 + N_I\right) - 1}{\left(1 + N_I\right)\left(1 - W_b\right)} \tag{A.4}$$

$$Q_{XT} = W_b/(W_b - 1)$$

$$N_I = v_P \Delta t / \Delta x$$

In equations (A.4) w_{CFL} is the Courant–Friedrichs–Lewy ratio (defined as $v_S\, \Delta t/\Delta x$, where $\Delta x \equiv \Delta x_1 = \Delta x_2 = \Delta x_3$) and W_b is a sensitivity factor (in numerical experiments presented and discussed in this paper we assume $W_b = 0.4$).

After the calculation of $\dot{\mathbf{U}}^m$ and $\mathbf{U}^m$ in regular (i.e., internal) nodes, particle velocity at time level m is calculated for nodes belonging to walls, following equations (A.1) and (A.2);

for nodes belonging to boundary edges $\dot{\mathbf{U}}^m$ is calculated as arithmetic average of values arising from the two walls of which the edges is the intersection. Finally, values in corners are obtained as arithmetic average of values coming from the three walls that have that corner in common. Updated particle displacement components at actual time level m are derived by numerical integration from updated particle velocity components.

References

Aagaard, B. T., and T. H. Heaton (2004), Near–source ground motions from simulations of substained intersonic and supersonic fault ruptures, *Bull. Seism. Soc. Am.*, *94*, No. 6, 2064–2078.

Abrahamson, N. and W. Silva (2008), Summary of the Abrahamson & Silva NGA ground motion relations, *Earthq. Spectra*, (in press).

Andrews, D. J. (1976a), Rupture propagation with finite stress in antiplane strain, *J. Geophys. Res.*, *81*, No. 20, 3575–3582.

Andrews, D. J. (1976b), Rupture velocity of plane strain shear cracks, *J. Geophys. Res.*, *81*, No. 32, 5679–5687.

Andrews, D. J. (1980), A stochastic fault model. 1. Static case, *J. Geophys. Res.*, *85*, No. B7, 3867–3877.

Antonioli, A., Belardinelli, M. E., Bizzarri, A., and K. S. Vogfjord (2006), Evidence of instantaneous dynamic triggering during the seismic sequence of year 2000 in South Iceland, *J. Geophys. Res.*, *111*, B03302, doi: 10.1029/2005JB003935.

Archuleta, R. J. (1984), A faulting model for the 1979 Imperial Valley earthquake, *J. Geophys. Res.*, *89*, 4559–4585.

Belardinelli, M. E., Bizzarri, A., and M. Cocco (2003), Earthquake triggering by static and dynamic stress changes, *J. Geophys. Res.*, *108*, No. B3, 2135, doi: 10.1029/2002JB001779.

Bernard, P., and D. Baumont (2005), Shear Mach wave characterization for kinematic fault rupture models with constant super–shear rupture velocity, *Geophys. J. Int.*, *162*, 431–447.

Bernard, P., and R. Madariaga (1984), A new asymptotic method for the modeling of near field accelerograms, *Bull. Seismol. Soc. Am., 74*, 539-558.

Bhat, H. S., Dmowska, R., King, G. C. P., Klinger, Y., and J. R. Rice (2007), Off–fault damage patterns due to supershear ruptures with application to the 2001 M_w 8.1 Kokoxili (Kunlun) Tibet earthquake, *J. Geophys. Res.*, *112*, B06301, doi: 10.1029/2006JB004425.

Bizzarri, A., and M. E. Belardinelli (2007), Modeling instantaneous dynamic triggering in a 3–D fault system: application to the June 2000 South Iceland seismic sequence, *submitted to Geophys. J. Intl.*.

Bizzarri, A., and M. Cocco (2003), Slip–weakening behavior during the propagation of dynamic ruptures obeying to rate– and state–dependent friction laws, *J. Geophys. Res.*, *108*, No. B8, 2373, doi: 10.1029/2002JB002198, ESE 3-1–ESE 3-21.

Bizzarri, A., and M. Cocco (2005), 3D dynamic simulations of spontaneous rupture propagation governed by different constitutive laws with rake rotation allowed, *Annals of Geophysics*, *48*, No. 2, 279–299.

Bizzarri, A., and M. Cocco (2006a), A thermal pressurization model for the spontaneous dynamic rupture propagation on a three–dimensional fault: 1. Methodological approach, *J. Geophys. Res.*, *111*, B05303, doi: 10.1029/2005JB003862.

Bizzarri, A., and M. Cocco (2006b), A thermal pressurization model for the spontaneous dynamic rupture propagation on a three–dimensional fault: 2. Traction evolution and dynamic parameters, *J. Geophys. Res.*, *111*, B05304, doi: 10.1029/2005JB003864.

Bizzarri, A., and M. Cocco (2006c), Comment on "Earthquake cycles and physical modeling of the process leading up to a large earthquake", *Earth, Planet and Space*, *58*, 1525–1528.

Bizzarri, A., Cocco, M., Andrews, D. J., and E. Boschi (2001), Solving the dynamic rupture problem with different numerical approaches and constitutive laws, *Geophys. J. Int.*, *144*, 656–678.

Boore, D. M., and G. A. Atkinson (2008), Ground motion prediction equations for the average horizontal component of PGA, PGV, and 5%–damped PSA at spectral periods between 0.01 s and 10.0 s, *Earthq. Spectra*, (in press).

Bouchon, M., Bouin, M. P., Karabulut, H., Toksoz, M. N., Dietrich, M., and A. J. Rosakis (2001), How fast is rupture during an earthquake? New insights from the 1999 Turkey earthquakes, *Geophys. Res. Lett.*, *28*, 2723–2726.

Bouchon, M., Toksoz, N., Karabulut, H., Bouin, M. P., Dietrich, M., Aktar, M., and M. Edie (2000), Seismic imaging of the 1999 Izmit (Turkey) rupture inferred from the near–fault recordings, *Geophys. Res. Lett.*, *27*, 3013–3016.

Bouchon, M., and M. Vallee (2003), Observation of long super–shear rupture during the magnitude 8.1 Kunlunshan earthquake, *Science*, *301*, 824–826.

Bouin, M.–P., and P. Bernard (1994), Analysis of strong motion S–wave polarization of the 15 October 1979 Imperial Valley earthquake, *Bull. Seism. Soc. Am., 84,* 1770–1785.

Broberg, K. B. (1994), Intersonic bilateral slip, *Geophys. J. Int.*, *119*, 706–714.

Broberg, K. B. (1995), Intersonic mode II crack expansion, *Arch. Mech.*, *47*, 859–871.

Burridge, R. (1963), The reflexion of a pulse in a solid sphere, *Proc. Roy. Soc. London A, 276,* 367–400.

Burridge, R. (1973), Admissible speeds for plane–strain self–similar shear cracks with friction but lacking cohesion, *Geophys. J. R. Astr. Soc.*, *35*, 439–455.

Burridge, R., and J. R. Willis (1969), The self–similar problem of the expanding elliptical crack in an anisotropic solid, *Proc. Camb. Phil. Soc.*, *66*, 443–468.

Campbell, K. C., and Y. Bozorgnia (2008), Campbell–Bozorgnia NGA horizontal ground motion model for PGA, PGV, PGD, and 5% damped linear elastic response spectra, *Earthq. Spectra*, (in press).

Chiou, B., and R. Youngs (2008), Chiou–Youngs NGA Ground motion relations for the geometric mean horizontal component of peak and spectral ground motion parameters, *Earthq. Spectra*, (in press).

Clayton, R., and B. Engquist (1977), Absorbing boundary conditions for acoustic anelastic wave equations, *Bull. Seism. Soc. Am.*, *67*, 1529–1540.

Cocco, M., and A. Bizzarri (2002), On the slip–weakening behavior of rate– and state–dependent constitutive laws, *Geophys. Res. Lett., 29*, No. 11, 11-1–11-4.

Das, S. (1981), Three–dimensional spontaneous rupture propagation and implications for the earthquake source mechanism, *Geophys. J. R. Astr. Soc.*, *67*, 375–393.

Das, S., and K. Aki (1977a), A numerical study of two–dimensional spontaneous rupture propagation, *Geophys. J. Roy. Astr. Soc.*, *50*, 643–668.

Das, S., and K. Aki (1977b), Fault plane with barriers: a versatile earthquake model, *J. Geophys. Res.*, *82*, No. 36, 5658–5670.

Day, S. M. (1982), Three–dimensional simulation of spontaneous rupture: the effect of nonuniform prestress, *Bull. Seism. Soc. Am.*, *72*, 1881–1902.

Day, S. M., Dalguer, L. A., Lapusta, N., and Y. Liu (2005), Comparison of finite difference and boundary integral solutions to three–dimensional spontaneous rupture, *J. Geophys. Res.*, *110*, B12307, doi: 10.1029/2005JB003813.

Delouis, B., Giardini, D., Lundgren, P., and J. Salichon (2002), Joint inversion of inSAR, GPS, teleseismic, and strong motions data for the spatial and temporal distribution of earthquake slip: application to the 1999 Izmit mainshock, *Bull. Seism. Soc. Am.*, *92*, 278–299.

Dunham, E. M. (2007), Conditions governing the occurrence of supershear ruptures under slip–weakening friction, *J. Geophys. Res.*, *112*, B07302, doi:10.1029/2006JB004717,

Dunham, E. M., and J. R. Archuleta (2004), Evidence for a super−shear transient during the 2002 Denali fault earthquake, *Bull. Seism. Soc. Am.*, *94*, No. 6B, S256–S268.

Dunham, E. M., and J. R. Archuleta (2005), Near–source ground motion from steady state dynamic rupture pulses, *Geophys. Res. Lett.*, *32*, L03302, doi: 10.1029/2004GL021793.

Ellsworth, W. L., Celebi, M., Evans, J. R., Jensen, E. G., Metz, M. C., Nyman, D. J., Roddick, J. W., Spudich, P., and C. D. Stephens (2004), Near–field ground motions of the *M* 7.9 November 3, 2002, Denali fault, Alaska, earthquake recorded at pump station 10, *Earthquake Spectra*, *20*, 597–615.

Emerman, S. H., and R. A. Stephen (1983), Comment on "Absorbing boundary conditions for acoustic and elastic wave equations" by R. Clayton and B. Engquist, *Bull. Seism. Soc. Am.*, *73*, 661–665.

Eshelby, J. D. (1949), Uniformly moving dislocations, *Proc. Phys. Soc. A*, *62*, 307–314.

Frankel, A., and R. W. Clayton, (1986), Finite difference simulations of seismic scattering Implications for the propagation of short–period seismic waves in the crust and models of crustal heterogeneity, *J. Geophys. Res.*, *91*, 6465–6489.

Freund, L. B. (1979), The mechanics of dynamic shear crack propagation, *J. Geophys. Res.*, *84*, 2199–2209.

Haskell, N. A. (1964), Total energy and energy spectral density of elastic wave radiation from propagating faults, *Bull. Seism. Soc. Am.*, *54*, 1811–1841.

Haskell, N. A. (1969), Elastic displacements in the near–field of a propagating fault, *Bull. Seism. Soc. Am.*, *59*, 865–908.

Heaton, T. H. (1990), Evidence for and implications of self–healing pulses of slip in earthquake rupture, *Phys. Earth Plan. Int.*, *64*, 1–20.

Higdon, R. L. (1991), Absorbing boundary conditions for elastic waves, *Geophysics*, *56*, 231–241.

Ida, Y. (1972), Cohesive force across the tip of a longitudinal–shear crack and Griffith' s specific surface energy, *J. Geophys. Res.*, *77*, No. 20, 3796–3805.

Johnson, T., Wu, T. F., and C. H. Scholz (1973), Source parameters for stick–slip and for earthquakes, *Science*, *179*, 278–280.

Joyner, W. B., and P. Spudich (1994), Including near–field terms in the isochrone integration method for application to finite–fault or Kirchhoff boundary integral problems, *Bull. Seismol. Soc. Am., 84*, 1260–1265.

Linker, M. F., and J. H. Dieterich (1992), Effects of variable normal stress on rock friction: observations and constitutive equations, *J. Geophys. Res.*, *97*, No. B4, 4923–4940.

Liu, P., Custodio, S., and R. J. Archuleta (2006), Kinematic inversion of the 2004 M 6.0 Parkfield earthquake including and approximation of the site effects, *Bull. Seism. Soc. Am.*, *96*, No. 4B, 143–158.

Madariaga, R. (1983), High frequency radiation from dynamics earthquake fault models, *Ann. Geophys.*, *1*, No. 17, 17–23.

Madariaga, R., and K. B. Olsen (2000), Criticality of rupture dynamics in 3–D, *Pure Appl. Geophys.*, *157*, 1981–2001.

Mai, P. M, and G. C. Beroza (2002), A spatial random field model to characterize complexity in earthquake slip, *J. Geophys. Res., 107*, 2308, doi:10.1029/2001JB000588.

Moczo, P. (1998), Introduction to modelling seismic wave propagation by Finite–Difference method – Lecture Notes, *Kyoto Univ.*

Ohnaka, M. (2003), A constitutive scaling law and a unified comprehension for frictional slip failure, shear fracture of intact rocks, earthquake rupture, *J. Geophys. Res.*, *108*, No. B2, 2080, doi: 10.1029/2000JB000123.

Okubo, P. G. (1989), Dynamic rupture modeling with laboratory–derived constitutive relations, *J. Geophys. Res.*, *94*, 12321–12335.

Olson, A. H., and R. J. Apsel (1982), Finite faults and inverse–theory with applications to the 1979 Imperial Valley earthquake, *Bull. Seism. Soc. Am.*, *72*, 1969–2001.

Peng, C., and M. N. Toksöz (1994), An optimal absorbing boundary condition for finite difference modelling of acoustic and elastic wave propagation, *J. Acoust. Soc. Am.*, *95*, 733–745.

Peng, C., and M. N. Toksöz (1995), An optimal absorbing boundary condition for elastic wave modelling, *Geophysics*, *60*, 296–301.

Reynolds, A. C. (1978), Boundary conditions for the numerical solution of wave propagation problems, *Geophysics*, *43*, 1099–1110.

Rice, J. R. (1993), Spatio–temporal complexity of slip on a fault, *J. Geophys. Res.*, *98*, 9885–9907.

Rosakis, A. J., Samudrala, O., and D. Coker (1999), Cracks faster than the shear–wave speed, *Science*, *284*, 1337–1340.

Roy, M., and C. Marone (1996), Earthquake nucleation on model faults with rate– and state– dependent friction: effects of inertia, *J. Geophys. Res.*, *101*, No. B6, 13,919–13,932.

Ruina, A. L. (1983), Slip instability and state variable friction laws, *J. Geophys. Res.*, *88*, No. B12, 10,359–10,370.

Savage, J. C. (1966), Radiation from a realistic model of faulting, *Bull. Seism. Soc. Am.*, *56*, 577–592.

Samudrala, O., Huang, Y., and A. J. Rosakis (2002), Subsonic and intersonic shear rupture of weak planes with a velocity weakening cohesive zone, *J. Geophys. Res.*, *107*, No. B8, 2170, doi 10.1029/2001JB000460.

Song, S. G., Beroza G. C., and P. Segall, (2007), A unified source model for the 1906 San Francisco Earthquake, *Bull. Seism. Soc. Am.*, in press.

Spudich, P., and E. Cranswick (1984), Direct observation of rupture propagation during the 1979 Imperial Valley earthquake using a short baseline accelerometer array, *Bull. Seism. Soc. Am.*, *74*, 2083–2114.

Spudich, P., and L. N. Frazer (1984), Use of ray theory to calculate high–frequency radiation from earthquake sources having spatially variable rupture velocity and stress drop, *Bull. Seism. Soc. Am.*, *74*, No. 6, 2061–2082.

Spudich, P., and D. Oppenheimer (1986), Dense seismograph array observations of earthquake rupture dynamics, in Earthquake Source Mechanics, Geophy. Monogr. 37, Am. Geophys., Un., ed. Das, S., Boatwright, J., and Scholz, C., 285–296.

Tinti, E., Bizzarri, A., and M . Cocco (2005), Modeling the dynamic rupture propagation on heterogeneous faults with rate– and state–dependent friction, *Annals of Geophysics*, *48*, No. 2, 327–345.

Wu, F. T., Thomson, K. C., and H. Kuenzler (1972), Stick–slip propagation velocity and seismic source mechanism, *Bull. Seism. Soc. Am.*, *62*, 1621–1628.

Xia, K., Rosakis, A. J., and H. Kanamori (2004), Laboratory experiments: the sub–Rayleigh-to-super–shear rupture transition, *Science*, *303*, 1859–1861.

Figure Captions

Figure 1. Particle velocity pulses radiated from a heterogeneous slip model having three different rupture time functions and the same slip velocity function ($\dot{f}_r(t) = \delta(t)$). Pulses calculated 14 km perpendicular to (0,0). Top row: uniform sub–shear rupture speed ($v_r = 0.9v_S$). Middle row: uniform super–shear rupture speed ($v_r = 1.5v_S$). Bottom row: rupture speed increases from sub–shear to super–shear, left to right. The slip distribution in this case is the same as in the previous two cases, but now the fault extent is smaller. Left column: slip model (colors) and contours of arrival time function (gray and black lines). Right column: ground velocity pulses (fault parallel component). Brackets show analysis window for calculating spectra.

Figure 2. Fourier amplitude spectra (FAS) of particle velocity pulses radiated from the three heterogeneous slip models in Figure 1. Sub–shear FAS is proportional to $1/f$, whereas both super–shear models (sustained super–shear propagation (dashes) and accelerating rupture speed, causing the saddle point (thin line)) have flat velocity spectra.

Figure 3. Schematic representation of the fault model used in this paper. The vertical plane $\mathcal{S}$ contains the fault Σ ($\Sigma \subseteq \mathcal{S}$) and $\hat{\mathbf{n}}$ is the unit vector normal to the fault. The total traction acting on the positive side of Σ is: $\mathcal{T}^{(\hat{\mathbf{n}})} = \mathbf{T}^{(\hat{\mathbf{n}})} + \mathbf{\Sigma}^{(\hat{\mathbf{n}})}$. The black star indicates the earthquake hypocenter H and dotted lines represent the ends of the computational spatial domain $\Omega^{(FD)}$.

Figure 4. Rupture speed on the fault plane in the case of model A, dry slip–weakening (see Table 1), calculated from equation (12). Blue portions of the fault identify the unbroken areas, while black star denotes the earthquake hypocenter; black triangles indicate the locations of the locations where FAS of fault slip velocity is calculated. Only for graphical clarity the rupture speed is calculated not in the whole temporal window of the computation, but only up to time $t = 1.29$ s.

Figure 5. FAS of the fault slip velocity time series in the nine locations displayed in Figure 4 for the dry slip–weakening model. Asterisks indicate locations where rupture speed is super–shear. Solid lines: unmodified FAS. Dashed and dotted lines: FAS of super–shear locations multiplied by ω and $\omega^{1/2}$, respectively. Vertical arrow shows the lowest frequency peak caused by numerical oscillation in slip velocity. "Not valid" shows the range of frequencies in which anti–plane and in–plane FAS cannot be compared owing to anti–plane numerical oscillation.

Figure 6. Slip velocity time series for three locations of each model. Columns left–to–right show models A, B, and C, respectively. Rows top–to–bottom show fault locations 1, 5 and 9, respectively. Gray line is original slip velocity function. Black line is the integrated tapered slip acceleration time series. Not shown is the effect of a final gradual taper applied to the integrated slip acceleration (black line).

Figure 7. The same as in Figure 4, but in case of temporally variable effective normal stress (model B; see Table 1). White portions on the fault are region where the rupture speed

exceeds the value of 4500 m/s. Only for clarity the rupture speed is calculated up to time $t = 1.21$ s.

Figure 8. FAS of the fault slip velocity time series in the nine locations displayed in Figure **7** for the thermal pressurization model. Asterisks indicate locations where rupture speed is super–shear. Solid lines: unmodified FAS. Dashed and dotted lines: FAS of super–shear locations scaled by ω and $\omega^{1/2}$, respectively. Vertical arrow shows the lowest frequency peak caused by numerical oscillation in slip velocity. "Not valid" shows the range of frequencies in which anti–plane and in–plane FAS cannot be compared owing to anti–plane numerical oscillation.

Figure 9. The same as in Figure 4, but in case of Dieterich–Ruina governing law (model C; see Table 1). Now the rupture velocity is displayed considering the whole time window considered.

Figure 10. FAS of the fault slip velocity time series in the nine locations displayed in Figure **9** for the rate and state and thermal pressurization model. Asterisks indicate locations where rupture speed is super–shear. Solid lines: unmodified FAS. Dashed and dotted lines: FAS of super–shear locations multiplied by ω and $\omega^{1/2}$, respectively. Vertical arrow shows the lowest frequency peak caused by numerical oscillation in slip velocity. "Not valid" shows the range of frequencies in which anti–plane and in–plane FAS cannot be compared owing to anti–plane numerical oscillation.

Figure 11. (a) Along strike–component of the shear stress on the fault at $t = 0$ in the case of model D (see Table 1). (b) Distribution of the resulting rupture times. Purple regions identifies fault patches where the initial shear stress overcomes the maximum yield stress and therefore region where rupture starts to nucleate. (c) Distribution of the rupture speed, again calculated using equation (12). White region emphasize fault nodes experiencing super–shear rupture velocity. (d) Comparison of average FAS of six sub–shear locations (blue line) and seven super–shear locations (red line), showing that the average sub–shear FAS has about twice the amplitude of the super–shear FAS in the 6–30 Hz band where the taper parameters permit a valid comparison. Coordinates of selected locations are listed (see Section 7 for details).

Tables

Table 1. Medium and constitutive parameters adopted in this study.

Parameter	Value		
	Medium and discretization parameters		
	Model A	**Models B and C**	**Model D**
$\lambda = G$	27 GPa		
v_P	5196 m/s		
v_S	3000 m/s		
ρ	3000 Kg/m^3		
$\Omega^{(FD)}$	box that extends 9010 m in x_1 direction, 300 m in x_2 and 9000 m in x_3	box that extends 5625 m in x_1 direction, 750 m in x_2 and 5600 m in x_3	box that extends 9020 m in x_1 direction, 3200 m in x_2 and 9000 m in x_3
Σ	{ $\mathbf{x}$ | $x_1 \in [60,8960]$ m, $x_2 = x_2^f = 150$ m, $x_3 \in [0,8950]$ m }	{ $\mathbf{x}$ |$x_1 \in [150,5500]$ m, $x_2 = x_2^f = 375$ m, $x_3 \in [0,5475]$ m }	{ $\mathbf{x}$ |$x_1 \in [120,8920]$ m, $x_2 = x_2^f = 1600$ m, $x_3 \in [0,8900]$ m}
$\Delta x_1 = \Delta x_2 = \Delta x_3 \equiv \Delta x$	10 m [a]	25 m [a]	20 m [a]
$f_{acc}^{(s)}$ [b]	50 Hz	20 Hz	25 Hz
Number of nodes in $\Omega^{(FD)}$	25 165 831	1 569 375	32 747 561
Δt	1.6970×10^{-4} s [a]	5.0649×10^{-4} s [a]	3×10^{-4} s [a]
ω_{CFL}	0.0509	0.0608	0.045
Number of time levels	20 000	2800	8000
$H \equiv (x_1^H, x_2^H, x_3^H)$	(4510,150,4500) m	(1125,375,4500) m	Patches where the yield stress is exceeded; see Section 7
t_{end}	3.38 s	1.42 s	2.4 s
v_l	0.01 m/s		
$\sigma_n^{eff} = \sigma_n - p_{fluid_0}^f$ (at $t = 0$)	30 MPa		
$\varphi(x_1, x_3, 0)$	0° [c]		
	Constitutive parameters		
	Model A	**Model B**	**Model C**	**Model D**
Governing law	Slip–weakening	Slip–weakening	Dieterich–Ruina	Slip–weakening

Variable effective normal stress (i.e., thermal pressurization included)	No	Yes	Yes	No
τ_0	20 MPa	20 MPa	19.2 MPa	Highly heterogen.; see Section 7 and Figure 11a
μ_u	0.93333	0.81667	-	0.93333
μ_f	0.33333	0.56667	-	0.33333
S (at $t = 0$)	0.8	1.5	-	Highly heterogen.; see Section 7
a	-	-	0.009	-
b	-	-	0.014	-
α_{LD}	-	-	0.53	-
d_0 (or L)	0.1 m	0.1 m	0.01 m	0.1 m

[a] This spatio–temporal discretization satisfies the convergence and stability conditions discussed BC05: their equation (A.4) gives 5.47 m $= \sqrt{3}\,\Delta x > v_P \Delta t = 0.88$ m for model A, 8.66 m $= \sqrt{3}\,\Delta x > v_P \Delta t = 2.63$ m for models B and C and 24.64 m $= \sqrt{3}\,\Delta x > v_P \Delta t = 1.56$ m for model D. From equations (A.5) of BC05 we have that the critical temporal and spatial sampling for model C are: $\Delta t^* = \dfrac{v_S\,\rho\,L}{4\omega_{CFL}(b-a)\sigma_n^{\ eff}} = 2.5$ s and $\Delta x^* = \dfrac{v_{S_{min}}^{\ 2}\,\rho\,L}{4\omega_{CFL}^{\ 2}(b-a)\sigma_n^{\ eff}} =$ 1.21×10^6 m, respectively (ω_{CFL} is the Courant–Friedrichs–Lewy ratio). Therefore both the continuum approximation conditions in (A.6) of BC05 are comfortably satisfied. See also Bizzarri and Cocco (2003) for a discussion of the convergency analysis.

[b] This is the value of the critical frequency up to which time series of waves propagating in the medium surrounding the fault are unaffected by oscillations due to spatial grid dispersion. For a regular point (i.e., not a split node) and for homogeneous medium this

frequency can be expressed as $f_{acc}^{(s)} = v_S/(6 \times \text{Max}\{\varDelta x_1, \varDelta x_2, \varDelta x_3\})$.

[c] As in BC05, the fault surface $\varSigma$ is oriented by means of the normal unit vector $\hat{\mathbf{n}} \mathbin{/\mkern-5mu/} \hat{\mathbf{e}}_2 \equiv (0,1,0)$ (see Figure 3) and the shear component $\mathbf{T}^{(\hat{\mathbf{n}})}$ of the traction $\mathcal{T}^{(\hat{\mathbf{n}})}$ is applied on the positive side of $\varSigma$, that is that extending in the direction of ascending x_2 coordinates. Therefore the adopted value of φ identifies a left–lateral fault.

Table 2. Rupture velocity in the nine locations considered models A to C presented and discussed in this study. The asterisk following the value of v_r indicates that it is super–shear.

Location #	Azimuth angle with respect to H	Absolute coordinates (x_1, x_3) (m)		Rupture velocity v_r (m/s)		
		Model A	Models B and C	Model A	Model B	Model C
1	0°	(7510,4500)	(4125,4500)	4209 *	5510 *	4099 *
2	− 11.25°	(7450,3900)	(4075,3900)	4047 *	4728 *	3902 *
3	− 22.5°	(7280,3340)	(3900,3350)	3460 *	4936 *	3629 *
4	− 33.75°	(7000,2820)	(3625,2825)	2734	4563 *	3291 *
5	− 45°	(6630,2370)	(3250,2375)	2724	4217 *	2945
6	− 56.25°	(6180,2000)	(2800,2025)	2803	2904	2584
7	− 67.5°	(5660,1720)	(2275,1725)	2612	2980	2456
8	− 78.75°	(5100,1550)	(1700,1550)	2553	2883	2584
9	− 90°	(4510,1500)	(1125,1500)	2561	2903	2468
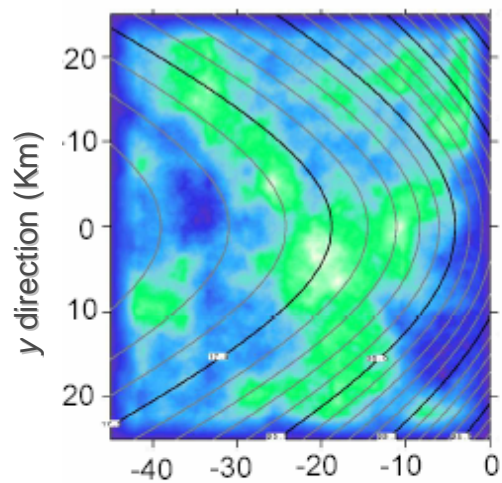
a) Subshear rupture velocity, no minimum or saddle point of arrival time
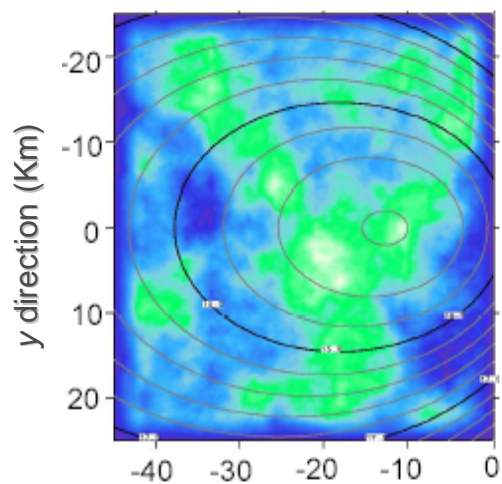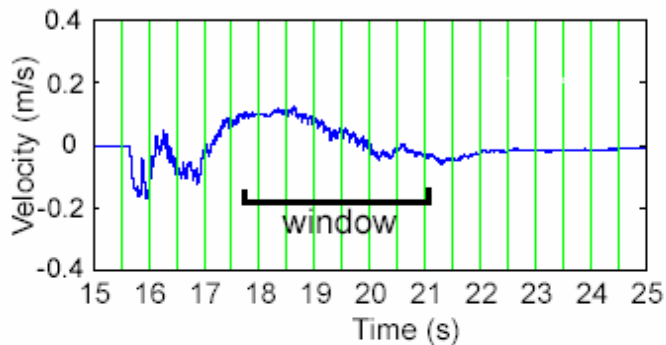
b) Supershear rupture velocity, local minimum in arrival time
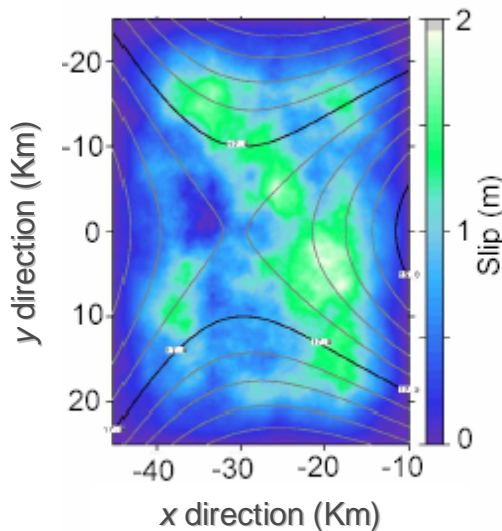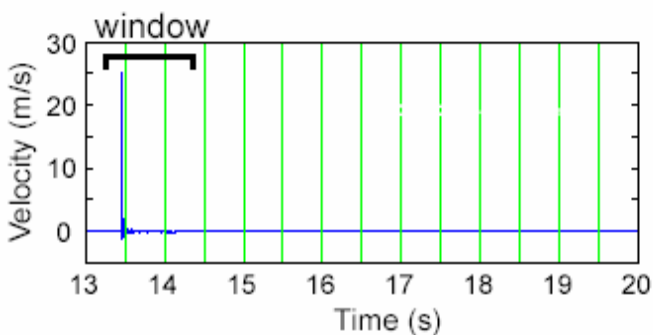
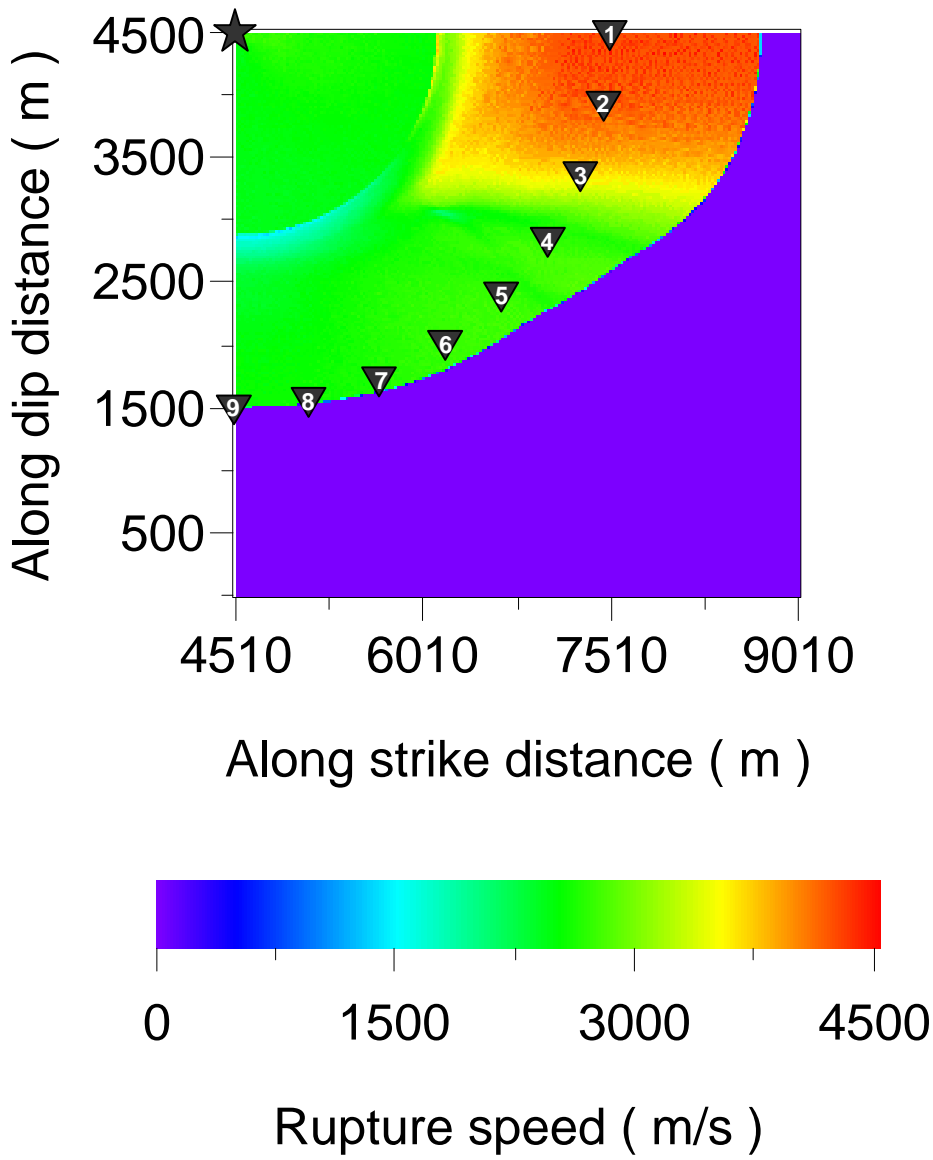c) Rupture accelerates to supershear, saddle point in arrival time

Figure 1

Figure 3

$$\sigma_{ij}^{eff} = \sigma_{ij} + p_{fluid}\delta_{ij}$$

$$\mathcal{T}_j^{(\hat{\mathbf{n}})} = n_i\sigma_{ij}^{eff}$$

$$\mathcal{T}^{(\hat{\mathbf{n}})} = \mathbf{T}^{(\hat{\mathbf{n}})} + \boldsymbol{\Sigma}^{(\hat{\mathbf{n}})}$$

$$T_j^{(\hat{\mathbf{n}})} = n_i\sigma_{ij}^{eff} - n_j(n_i\sigma_{ik}^{eff}n_k)$$

$$\Sigma_j^{(\hat{\mathbf{n}})} = n_j(n_i\sigma_{ik}^{eff}n_k)$$

In our geometry:

$$\hat{\mathbf{n}} \; // \; \hat{\mathbf{x}}_2 \equiv (0,1,0)$$

$$\mathbf{T}^{(\hat{\mathbf{n}})} = (\sigma_{21},0,\sigma_{23})$$

$$\boldsymbol{\Sigma}^{(\hat{\mathbf{n}})} = (0,-\sigma_n^{eff},0)$$

$$\sigma_n^{eff} = \sigma_n - p_{fluid} = -\sigma_{22} - p_{fluid}$$

Figure 4

Along dip distance (m)

Along strike distance (m)

Rupture speed (m/s)
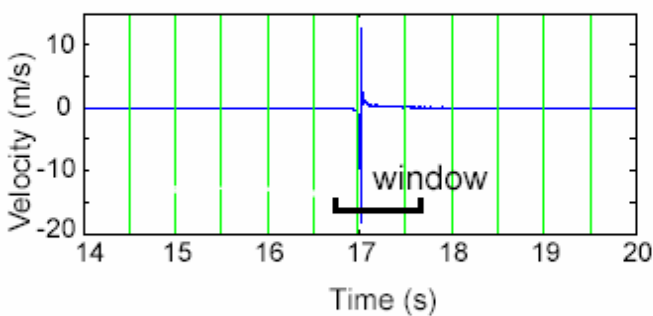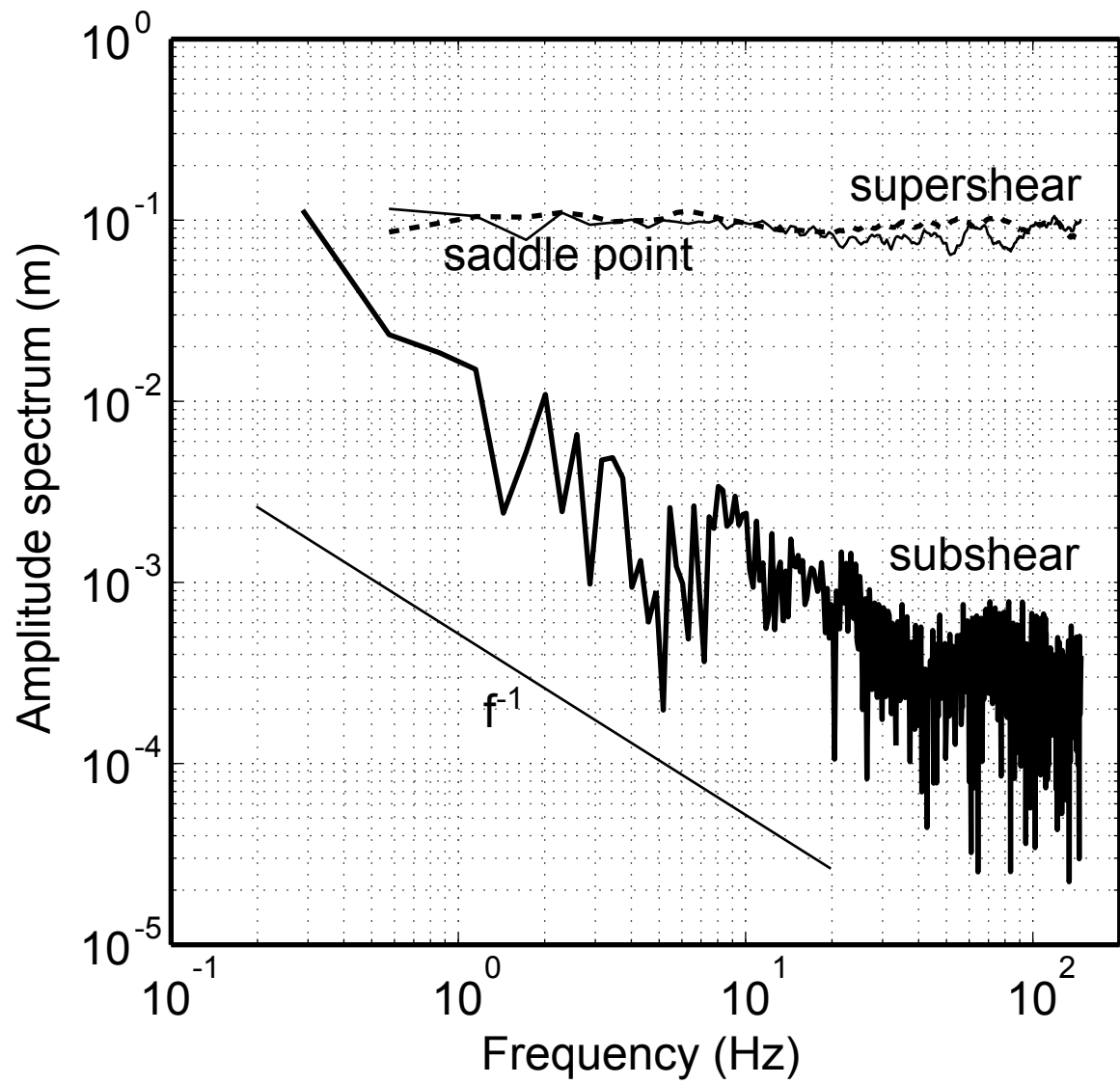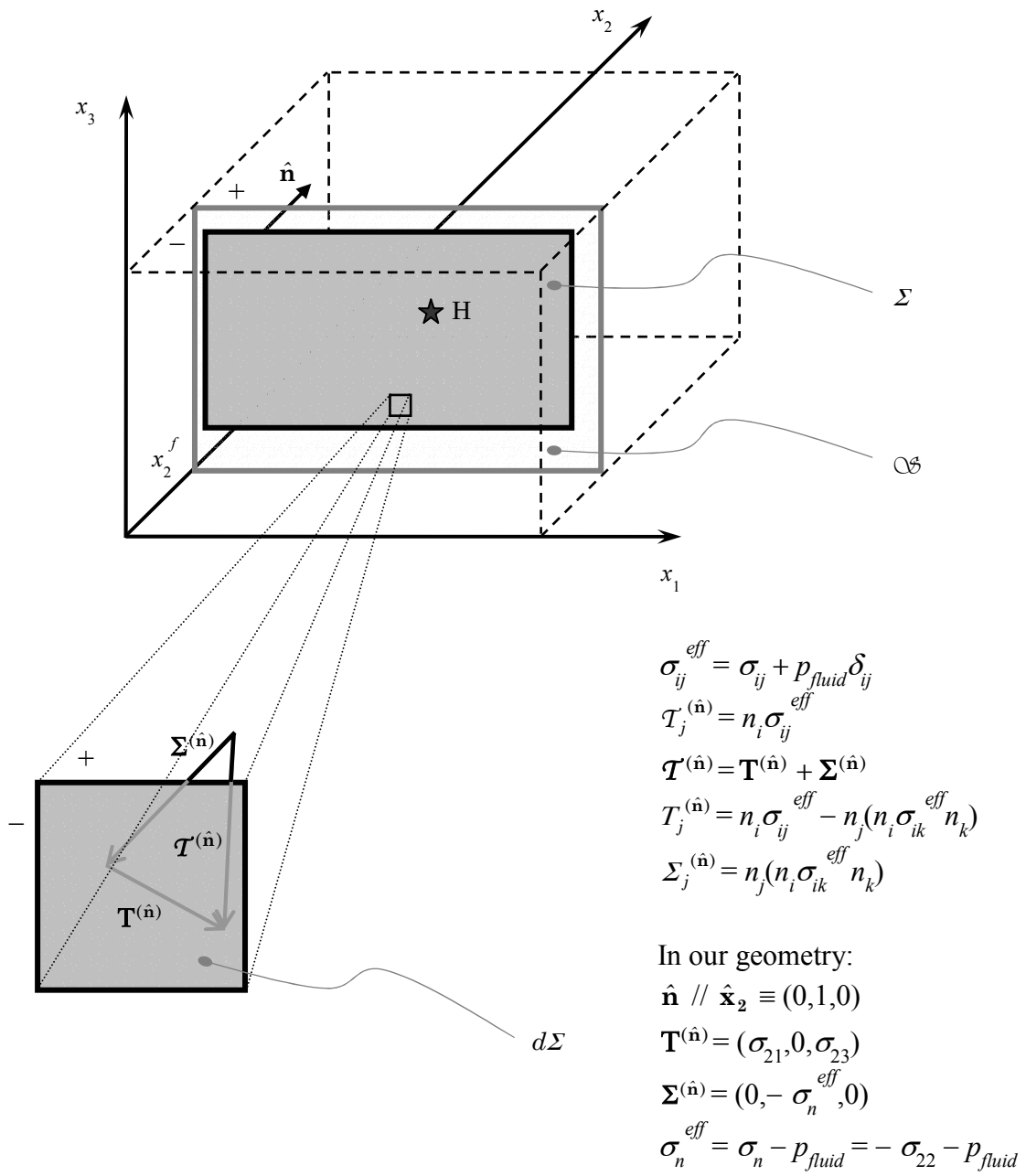
Slip velocity spectra, slip weakening model, S=0.8, dry

Slip velocity (m/s)

Time (s)
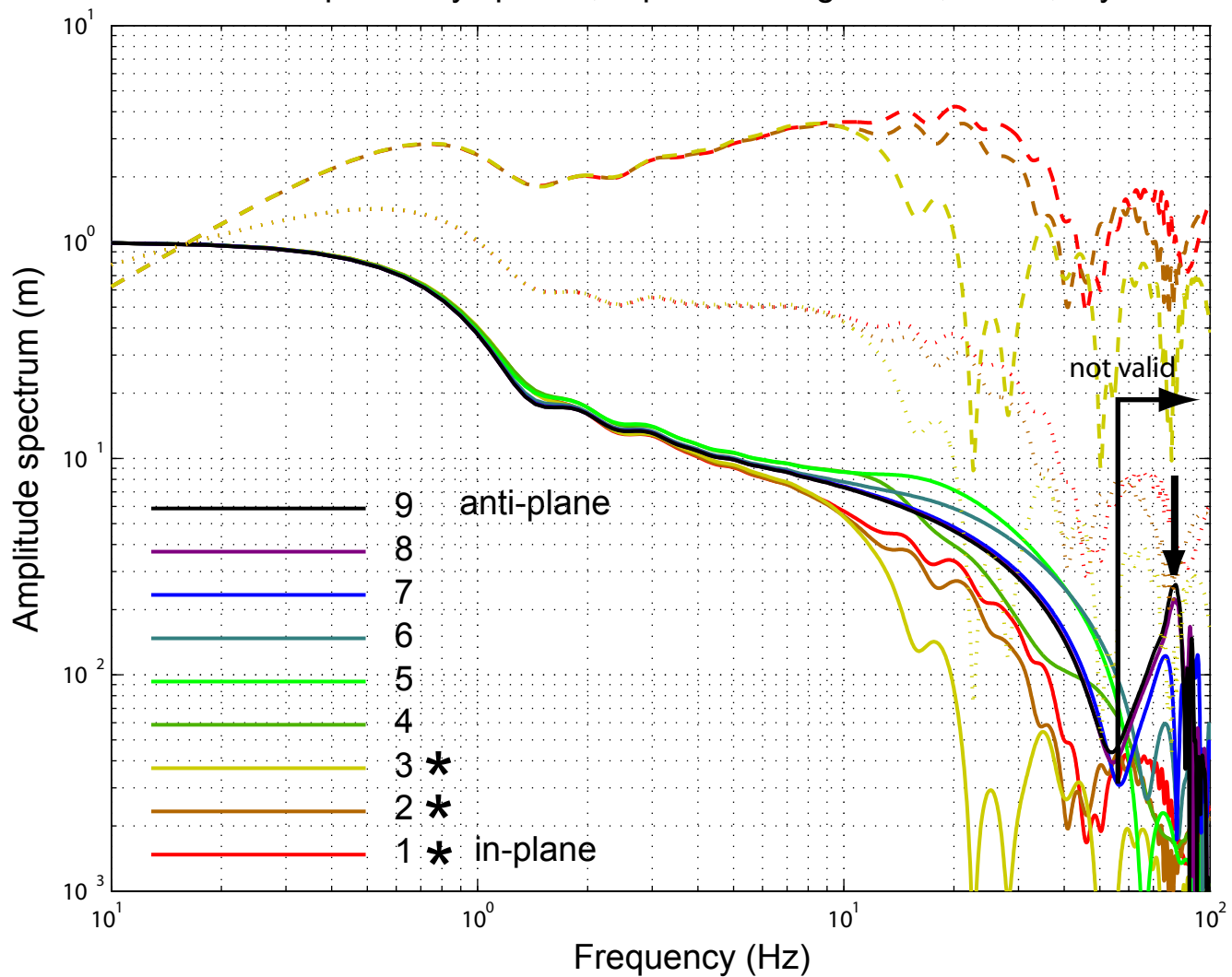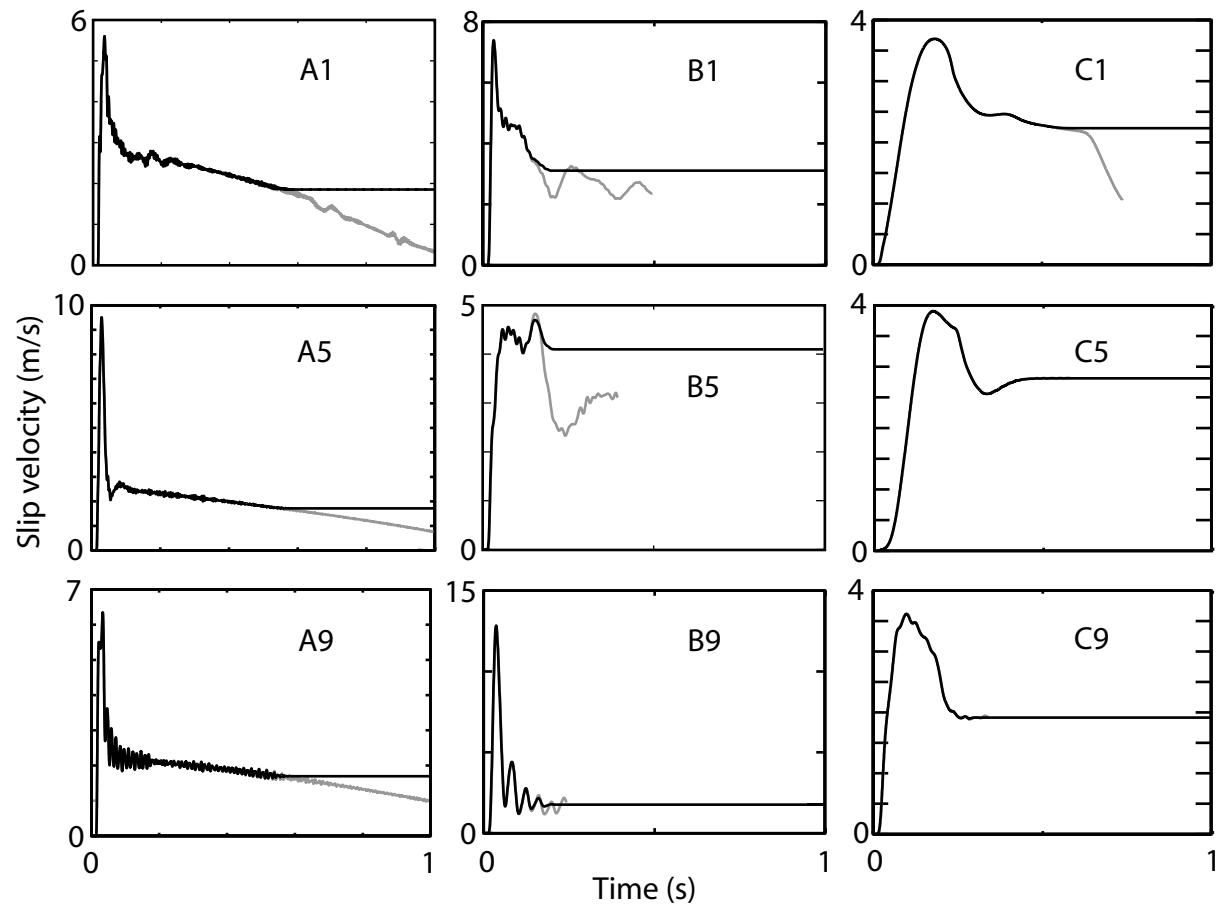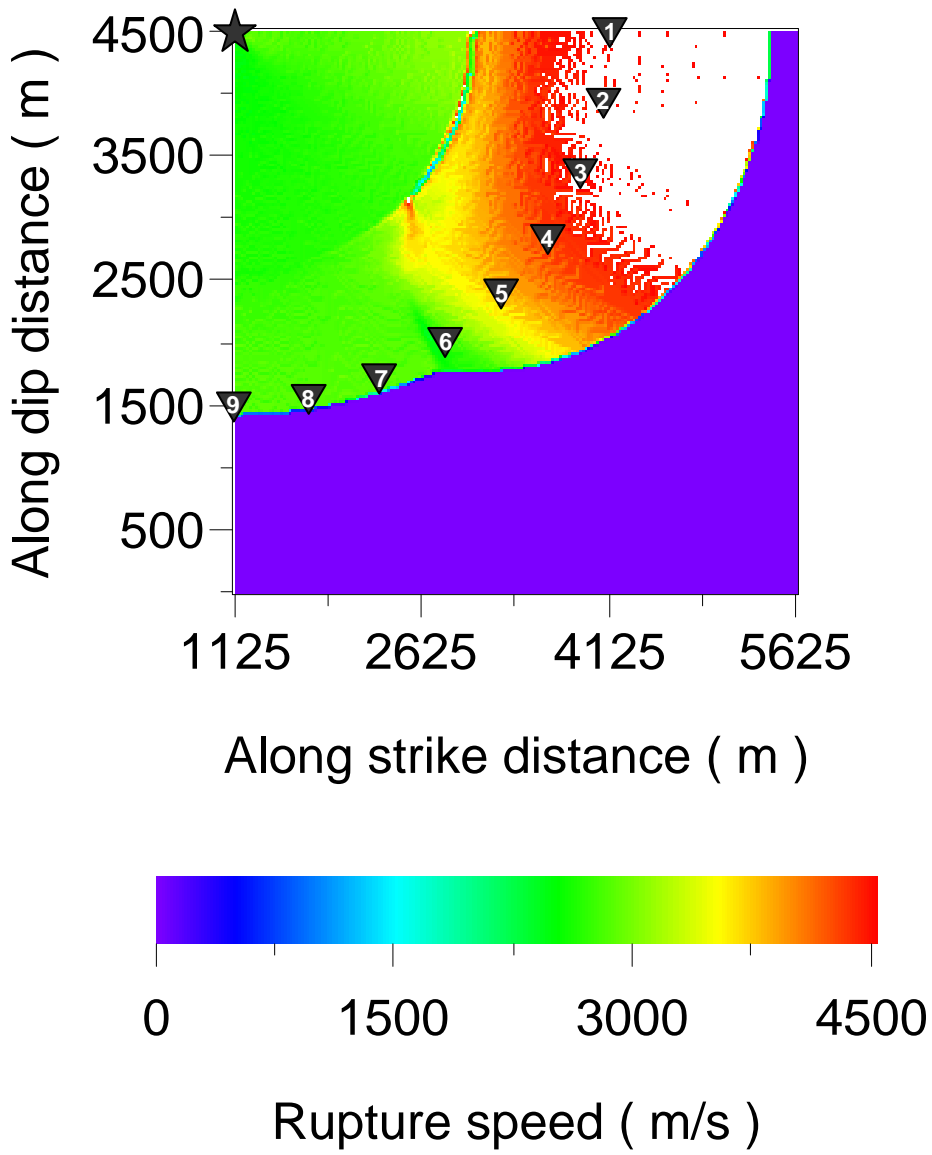
Figure 7

Slip velocity spectra, thermal pressurization model
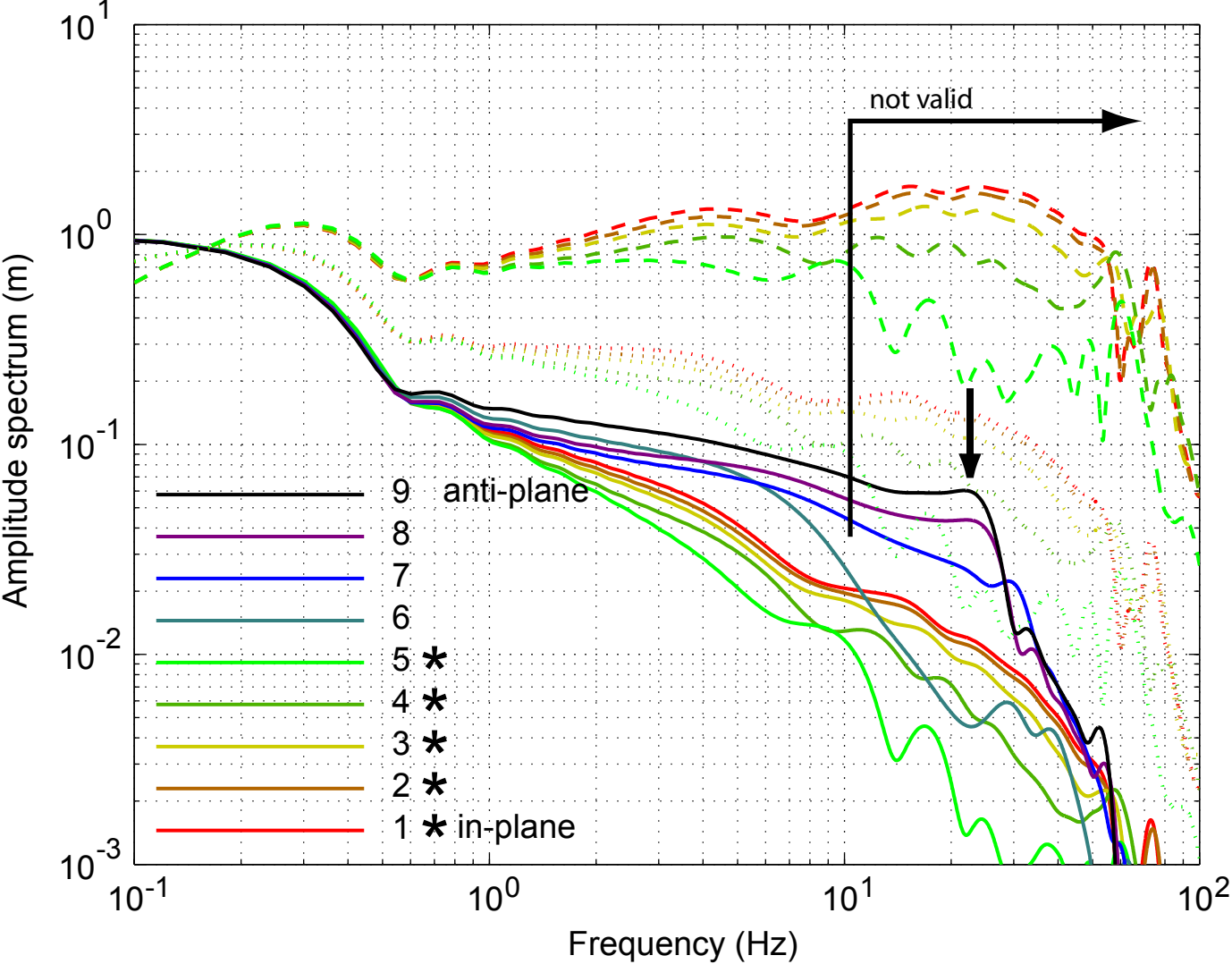
Figure 9
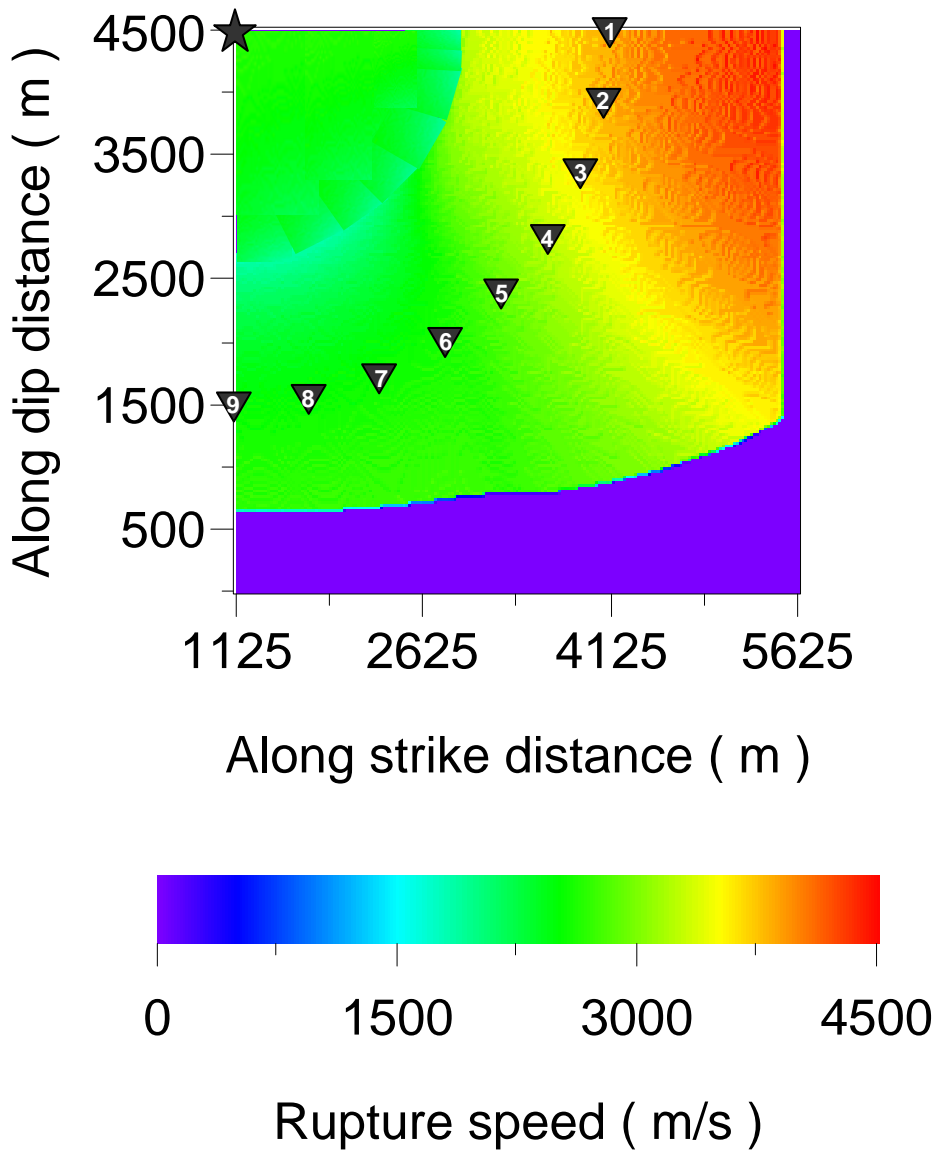
Slip velocity spectra, rate-state friction, wet

Figure 11

(a)

(b)
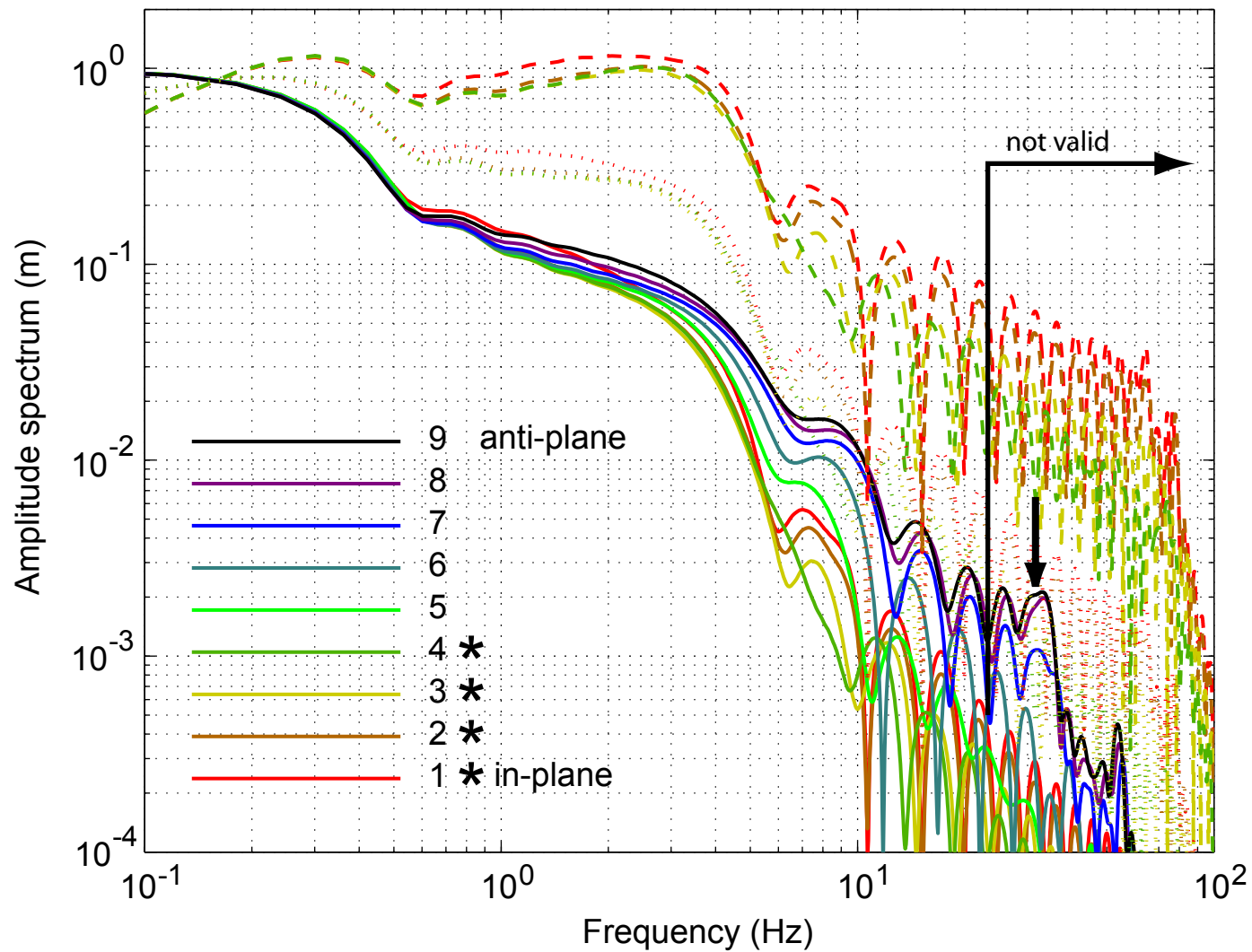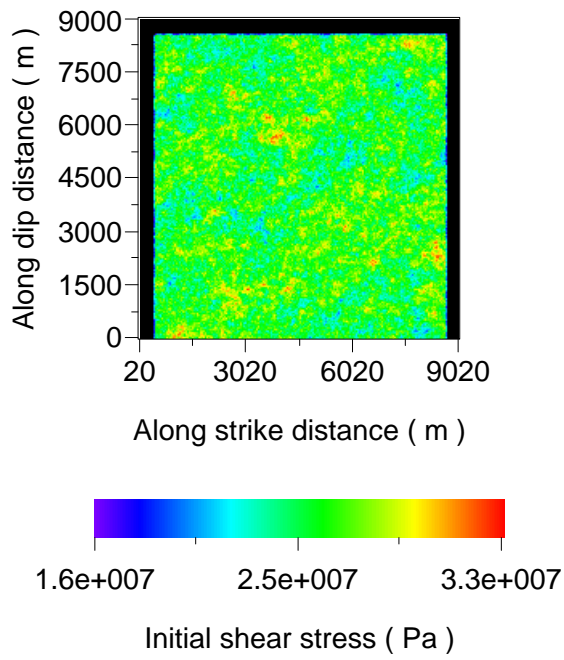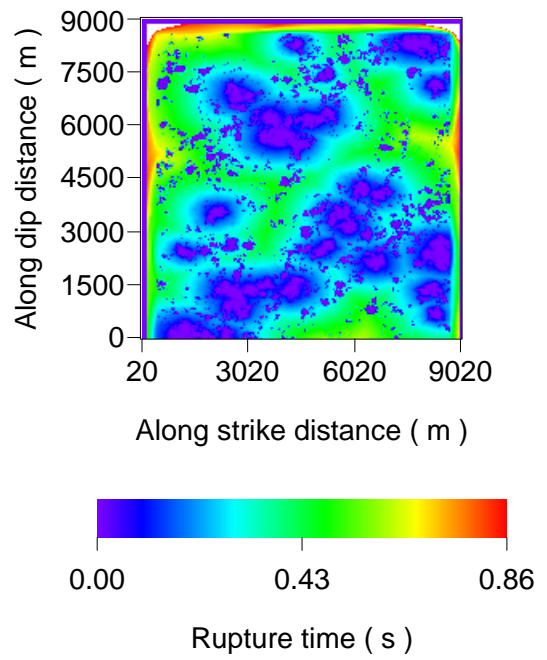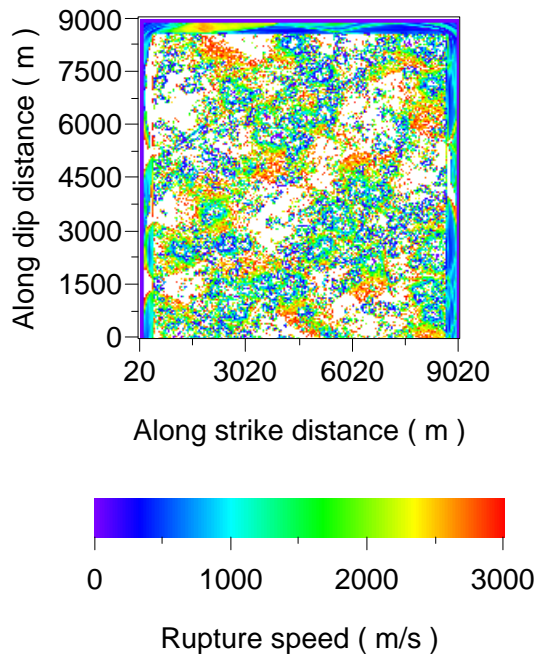

(c)

(d)